8-24-2002

Correlation Between Volcanic and Tectonic Segmentation of Fast-Spreading Ridges: Evidence from Volcanic Structures and Lava Flow Morphology on the East Pacific Rise at 9°-10°N

Scott M. White
University of South Carolina - Columbia, swhite@geol.sc.edu

Rachel M. Haymon
University of California - Santa Barbara

D J. Fornari

Michael R. Perfit
University of Florida

Ken C. Macdonald
University of California - Santa Barbara

Publication Info

Published in *Journal of Geophysical Research*, Volume 107, Issue B8, 2002, pages 1-20.
White, S. M., Haymon, R. M., Fornari, D. J., Perfit, M. R., Macdonald, K. C. (2002). Correlation between volcanic and tectonic segmentation of fast-spreading ridges: Evidence from volcanic structures and lava flow morphology on the East Pacific Rise at 9°-10°N. *Journal of Geophysical Research, 107* (B8), 1-20.

Correlation between volcanic and tectonic segmentation of fast-spreading ridges: Evidence from volcanic structures and lava flow morphology on the East Pacific Rise at 9°–10°N

Scott M. White,[1,2] Rachel M. Haymon,[1] Daniel J. Fornari,[3] Michael R. Perfit,[4] and Ken C. Macdonald[1]

Received 19 April 2001; revised 15 January 2002; accepted 20 January 2002; published 24 August 2002.

[1] Combined analyses of volcanic features in DSL-120 sonar data and *Argo I* images along the ridge crest of the East Pacific Rise, 9°09′–54′N reveal a consistent decrease in inferred lava effusion rate toward the ends of third-order segments. The correlation of tectonic segmentation and volcanic style suggests that third-order segmentation corresponds to the volcanic segmentation of the ridge. Along-axis changes in volcanic structures (from collapse troughs to basaltic lava domes) and lava morphology (from sheet to pillow flows) coincide with the boundaries of morphologically defined third-order tectonic segments of the ridge crest visible in shipboard multibeam bathymetry. Pillow lava flows cover 25% of the surveyed area of the ridge crest and are closely associated with small lava domes that occur primarily at third-order segment ends. An additional 25% of the surveyed area of the ridge crest is covered by sheet lava flows found in close association with an axial collapse trough. The remaining terrain consists of lobate lava flows. We interpret the spatial correlations of morphologic, structural, seismic, and petrologic data as evidence that individual volcanic plumbing systems are organized at ~20 km spacing along the ridge axis (third-order segment scale) in agreement with the hypothesis that volcanic and tectonic segmentations are correlated. For fast spreading ridges, we estimate that the longevity of volcanic segments is $\sim 10^4$–10^5 years, 1–3 orders of magnitude longer than fourth-order segments ($\sim 10^2$–10^3 years). This implies the present pattern of hydrothermal activity may reorganize tens or hundreds of times while volcanic segmentation remains fairly stable. *INDEX TERMS:* 3040 Marine Geology and Geophysics: Plate tectonics (8150, 8155, 8157, 8158); 3035 Marine Geology and Geophysics: Midocean ridge processes; 8429 Volcanology: Lava rheology and morphology; 3045 Marine Geology and Geophysics: Seafloor morphology and bottom photography; 9355 Information Related to Geographic Region: Pacific Ocean; *KEYWORDS:* ridge axis, neovolcanic, seafloor, segmentation, volcanism

1. Introduction

[2] Understanding the causes of along-strike changes in eruptive processes provides important insights into the formation of new oceanic crust at fast spreading ridges. In this study, we relate observations of volcanic structures and lava morphology from near-bottom acoustic and visual data to the structural segmentation of the East Pacific Rise (EPR) from 9° to 10°N, and show how eruptive processes vary along the axis of this fast spreading (~11 cm/yr full rate) ridge. Then, we combine the visual, sonar, petrological, and geophysical data to discuss the nature of volcanic systems on the EPR.

[3] The concept of a volcanic system is useful in mid-ocean ridge volcanology, especially for the EPR where the term ''volcano'' may be misleading due to its common use as a synonym for volcanic edifice [*Simkin and Siebert*, 2000]. In contrast to most volcanoes, the EPR does not build large volcanic edifices at the ridge axis, instead the topographic rise is caused by flexural or isostatic forces [*Eberle and Forsyth*, 1998; *Madsen et al.*, 1986]. The set of fissures, dikes, and crater rows developed along rift in association with a central volcano is commonly referred to as a volcanic system in Iceland [e.g., *Gudmundsson*, 1995]. The essential point is that the features within a volcanic system share a common volcanic plumbing system. We apply this usage of volcanic system to the EPR.

[4] Volcanic segments of the EPR are individual volcanic systems bounded by discontinuities analogous to intervolcano gaps. Previous work on the southern EPR (SEPR) (17°–18.5°S) led to the conclusion that volcanic segmentation corresponds to third-order structural segmentation, such that each volcanic segment contains a single volcanic

[1]Department of Geological Sciences and Marine Science Institute, University of California, Santa Barbara, California, USA.
[2]Now at Department of Geological Sciences, University of South Carolina, Columbia, South Carolina, USA.
[3]Department of Geology and Geophysics, Woods Hole Oceanographic Institution, Woods Hole, Massachusetts, USA.
[4]Department of Geological Sciences, University of Florida, Gainesville, Florida, USA.

0148-0227/02/2001JB000571$09.00

Table 1. Third-Order Ridge Axis Discontinuity Zones Picked From Ridge Axis Offsets and Saddles Visible in Multibeam Bathymetry 10 m Contour Maps to nearest 0.5′ (0.9 km)[a]

Latitude Bounds of Discontinuity Zone	Size and Sense of Offset[b]		How Offsets Were Previously Noted	Seismic AMC Discontinuity
	Multibeam	DSL-120		
9°58′N 9°51.5′N	bathymetric saddle point (−20 m)	15–20 m deep saddle without distinct lateral offset, location of ridge axis imprecise ±250 m		break [*Detrick et al.*, 1987; *Vera and Diebold*, 1994]
9°45′N 9°43.5′N	0.5 km right offset of axis through Saddle Point (−10 m)	0.3–0.5 km right translation of axis from a ∼50 m wide, ∼20 m deep ASCT at 9°45′N through a zone of right-stepping en echelon fissures that merge into a ∼400 m wide, ∼20 m deep ASCT at 9°43.5′N	ASCT becomes zone of fissures [*Haymon et al.*, 1991] 0.5 km right step in SeaMARC II, part of en echelon series of offsets [*Macdonald et al.*, 1992]	pinch-down in width, depth increase [*Kent et al.*, 1993a]
9°38′N 9°36.5′N	0.5 km right step of axis, no depth change	<0.5 km right step without depth change, between 2 overlapping ∼200 m wide, ∼20 m deep ASCTs	several en echelon offsets of ASCT from SeaMARC II, [*Macdonald et al.*, 1992] ASCT overlap, [*Haymon et al.*, 1991]	pinch-down, possible break [*Kent et al.*, 1993a; *Toomey et al.*, 1990]
9°21′N 9°19′N	∼1 km right stepping overlap of <10 m topographic highs marking axes	>0.5 km right stepping overlap of local topographic high (20 m) from south and >200 m wide zone of fissures and collapses from north	1 km right-step, [*Macdonald et al.*, 1992] possible fourth-order offset and lava-age transition boundary [*Haymon et al.*, 1991]	MCS off axis here width discontinuity across offset- double reflection? [*Kent et al.*, 1993b]
9°12′N 9°08′N	0.5 km right offset of axis through saddle point (−20 m)	0.5 km right stepping overlap of two local topographic ridges (200–400 m wide, >30 m high)	0.5 km right-step, [*Macdonald et al.*, 1992] possible fourth-order offset [*Haymon et al.*, 1991]	break in AMC [*Detrick et al.*, 1987; *Kent et al.*, 1993b]

[a] The supporting data are independent of offsets picked.
[b] For multibeam bathymetry maps (100 m grid, 10 m contours) and DSL-120 bathymetry maps (4 m grid, 5 m contours).

system [*White et al.*, 2000]. This conclusion is strengthened by observations of spatial correlations between third-order ridge axis offsets discontinuities in the seismic structure of the EPR ridge crest at 15.5°–17°N [*Carbotte et al.*, 2000]. Here we demonstrate that third-order segmentation corresponds to volcanic segmentation on the EPR at 9°–10°N.

[5] Third-order segmentation on the fast spreading EPR is morphologically defined by discontinuity in the overall structure of the axial topographic high. At a minimum, this consists of >200 m offset in the continuous linear axial trace, or a significant (>20 m) bathymetric saddle accompanied by narrowing the breadth of the axial high (Table 1). This definition differs slightly from that proposed by *Macdonald et al.* [1992] as explained in detail by *White et al.* [2000]. All third-order segment boundaries were picked solely from the multibeam bathymetry (Figure 1). Several generations of regional bathymetry have been produced for the EPR between the 9°03′N overlapping spreading center (OSC) and Clipperton fracture zone [*Cochran et al.*, 1999; *Macdonald et al.*, 1992; *Wilcock et al.*, 1993; D. J. Fornari, WHOI, 2000]. For most of the study area, we used a 100 m grid of *Cochran et al.* [1999] to identify third-order segments. This grid does not extend the full length of our study area, so we combined the bathymetry from *Cochran et al.* [1999] and *Carbotte and Macdonald* [1992] to pick the remainder of the segments in the study area. Subsequently, the DSL-120 sonar records collected in March 2000 were used to refine these picks to 900 m (0.5′) precision. Fissure swarms, the axial summit collapse trough (ASCT), and smaller collapse pits visible on the DSL-120 records establish a continuous axial trace that we are able to follow into fine-scale overlap zones that are below the resolution of the multibeam bathymetry maps. Note that re-picking the segment ends from DSL-120 records improves only the precision of their initial positions from multibeam bathymetry, not their accuracy.

[6] EPR morphology at 9°–10°N is typical of fast spreading ridges [*Carbotte and Macdonald*, 1994]. Multibeam bathymetry reveals that the first-order ridge segment between the Clipperton and Siquieros transform faults is offset by the 9°N OSC, a second-order offset [*Macdonald et al.*, 1992]. Within the second-order segment from the OSC at 9°N to the Clipperton transform, the ridge axis maintains a minimum depth in the range of 2500–2600 m. The general cross-sectional shape of the axial region changes abruptly from a narrow, triangular ridge crest at the ridge intersection with the Clipperton to a broad rectangular axial high, maintains this rectangular cross-sectional shape for half the segment, then gradually tapers southward to a domal and then a triangular shape approaching the 9°N OSC [*Macdonald and Fox*, 1988]. The calculated cross-sectional area of the axial high exhibits the same pattern of abrupt increase in axial cross-section south of the Clipperton and subsequent gradual decrease southward to the 9°N OSC [*Scheirer and Macdonald*, 1993]. Two significant

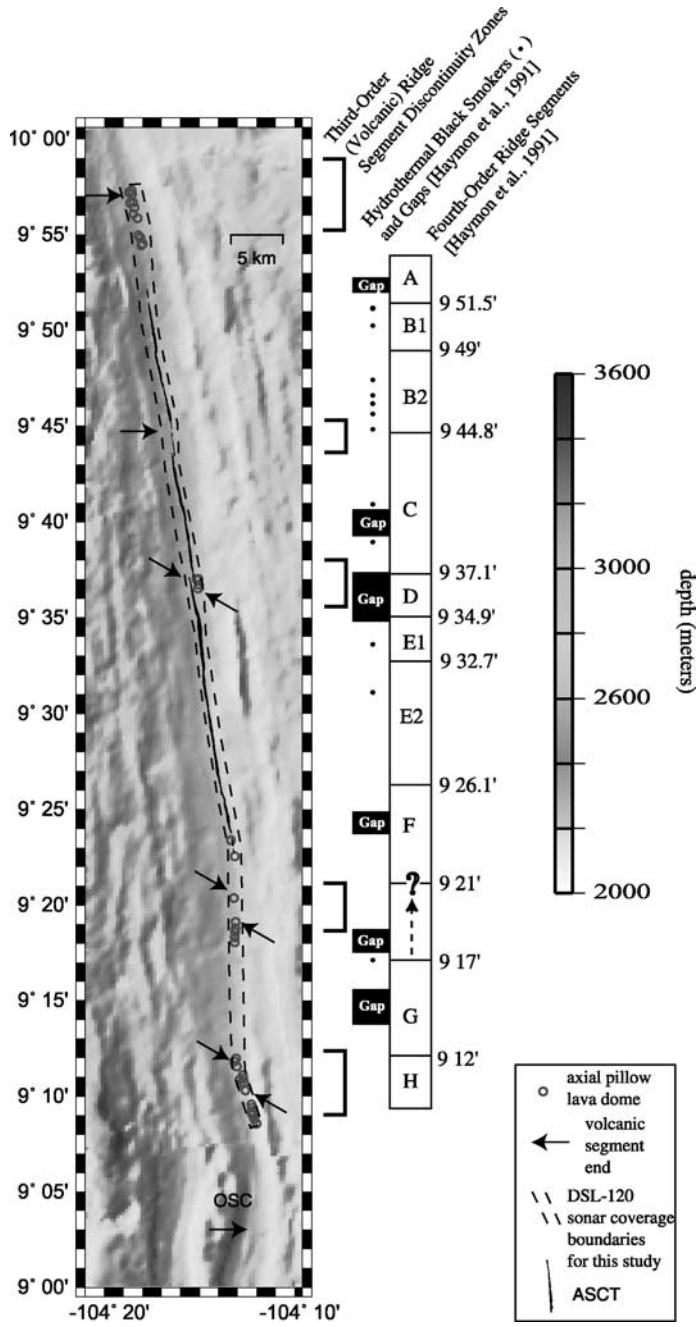

Figure 1. Map of the study area with bathymetry shown in shaded relief illuminated from the west. Arrows show the endpoints of third-order (volcanic) segments and are angled so that southeast pointing arrows mark the north end of a segment and northwest pointing arrows mark the south end of a segment. The areas between arrows are very small overlap zones between ridge axes. The axial summit collapse trough (ASCT) modified from *Haymon et al.* [1991] is outlined in black. The two largest offsets in the ASCT correspond to third-order segment ends. The limits of the DSL-120 sonar coverage area are outlined by solid black line. The pillow lava domes found in the axial zone (shown as small open circles) are found exclusively near the volcanic segment ends. (left) The discontinuity zones between the third-order segments (indicated by brackets). (middle) The black boxes labeled ''gap'' show where no evidence for hydrothermal activity was seen using *Argo* in 1989, and black dots show where black smoker chimneys or smoke plumes were seen in 1989 [*Haymon et al.*, 1991]. (right) The fourth-order ridge segments in the 1989 *Argo* survey area [*Haymon et al.*, 1991]. *Haymon et al.* [1991] expressed uncertainty about the location of the F/G segment boundary as indicated by the dashed arrow. Most third-order segments contain multiple fourth-order segments.

local minima in the cross-sectional area are particularly apparent at 9°57′N and 9°21′N [*Scheirer and Macdonald*, 1993] also correspond to two third-order segment boundaries identified herein.

[7] In addition to multibeam bathymetry, the EPR at 9°–10°N is the site of many other studies critical to understanding the nature of the volcanic systems along fast spreading ridges. The *Argo I* photoacoustic sled was used to survey the ridge crest from 9°09′–54′N in 1989 [*Haymon et al.*, 1991]. The 1989 Argo I survey provides detailed lava morphology observations used here, and information on hydrothermal distribution, tectonic features and very high-resolution 100 kHz sonar images [*Fornari et al.*, 1998; *Haymon et al.*, 1991; *Wright et al.*, 1995]. The DSL-120 side-scan sonar system was used to survey the ridge crest from 9°08′–10°02′N in March 2000. We use DSL-120 data to examine the mesoscale ridge crest structures such as: axial lava mounds, ASCT segments, fissure swarms, and lava distribution systems (tubes and channels). Numerous rock sample analyses indicate variability in the magmatic system within the second-order segment [*Batiza and Niu*, 1992; *Langmuir et al.*, 1986; *Perfit et al.*, 1994; *Smith et al.*, 2001]. Several studies of the seismic structure of the axial region provide a means for correlating our seafloor observations to seismic characteristics of the magmatic system [*Detrick et al.*, 1987; *Dunn et al.*, 2000; *Harding et al.*, 1993; *Kent et al.*, 1993a, 1993b; *Toomey et al.*, 1994; *Vera and Diebold*, 1994].

2. Volcanic Structures Imaged by DSL-120 Sonar

2.1. Data Acquisition

[8] Volcanic structures formed on the ridge crest of the EPR are commonly tens to hundreds of meters long, inconveniently falling between the optimum resolution of sea surface sonar systems (~100 m pixel resolution) and mixed optical-acoustic observations from occupied submersibles and remotely operated vehicles (~20 m total swath width). Prior to 2000, side-scan sonar data of the study area consisted of SeaMARC II coverage of the ridge axis [*Macdonald et al.*, 1984], a short SeaMARC I swath between the Clipperton and 9°54′N [*Kastens et al.*, 1986], and multiple ~300 m wide swaths of *Argo I* 100 kHz sonar from 9°54′N to 9°08′N [*Fornari et al.*, 1998]. In 2000, DSL-120 side-scan sonar and phase bathymetry data were obtained continuously along the ridge axis from 9°08′–10°N (Figure 1). The DSL-120 sonar survey provides complete coverage at the intermediate scale needed to clearly resolve the volcanic structures on the EPR crest.

[9] The DSL-120 sonar operates at 120 kHz and has an effective near-nadir pixel resolution of 1 m for side-scan backscatter imagery and 4 m for phase bathymetry, when towed at ~1 knot at ~100 m altitude [*Scheirer et al.*, 2000]. Under these conditions, we obtained a 900–1000 m wide backscatter reflectivity swath and a 700–800 m wide bathymetry swath. Two overlapping parallel lines were run from 10°02′N to 9°36′N, and one line was continued south to 9°08′N. A perpendicular crossing line was run at 9°37′N. Neither the crossing line nor the overlapping areas showed any systematic bias in the bathymetry values after processing. The side scan backscatter reflectivity measures the amplitude of the acoustic return, which appears to be primarily influenced by the slope and roughness of seafloor in axial zones for 120 kHz sound [*Scheirer et al.*, 2000; *Stewart et al.*, 1994]. Bottom-moored transponder navigation was available from 9°34′N to 9°38′N. Navigation for the rest of the survey was determined by a layback correction for the DSL-120 towfish position calculated from ship speed and the length of wire paid out relative to P-code GPS defined ship position. Comparison of distinctive features in overlapping DSL-120 swath indicates that the layback navigation was self-consistent to within ~100 m. Prior work with the bottom-moored transponders indicates that they are accurate to within 5–10 m in global geodetic navigational coordinates [*Fornari et al.*, 1998].

2.2. Observations of Volcanic Structures

[10] Lava mounds and collapse troughs are the two most well defined volcanic structures in DSL-120 sonar data (Figure 2). In addition, we interpret several low-reflectivity areas in the DSL-120 backscatter imagery and long sinuous collapses in the DSL-120 backscatter and bathymetry as lava channels based on their morphology, proximity to areas of previously observed lava channels [*Fornari et al.*, 1998; *Haymon et al.*, 1991], and association with sheet lava flows. Axial lava mounds, collapse troughs, and lava channel systems are the same volcanic structures that were identified in the 1996 DSL-120 survey on the southern EPR [*White et al.*, 2000].

[11] Dominating the axial zone from 9°52′N to 9°23′N, the ASCT appears as a series of long, narrow depressions in the DSL-120 bathymetry, and as paired weak-strong backscatter reflections with the weaker reflection nearest to the sonar towfish (Figure 2). In our study area, the ASCT may be divided into three distinct collapse structures, which correspond to three of the third-order segments picked from multibeam bathymetry. A narrow ASCT segment, ~50 m wide and ~10–20 m deep from 9°45′N to 9°52′N, is separated across a zone of small-scale collapse and fissuring from a wider ASCT segment, ~400 m wide and ~20 m deep from 9°43.5′N to 9°36.4′N. A similar wide ASCT segment begins at a right step overlapping offset at 9°37.9′N and continues to 9°23′N (Table 1). Lava channels emanating from the ASCT indicate high effusion rate eruptions and transport of lava at least a few hundred meters down the ridge flanks. Previous studies have provided detailed descriptions of the ASCT in our study area [*Fornari et al.*, 1998; *Haymon et al.*, 1991].

[12] Lava mounds appear as quasi-circular paired reflections in the backscatter data indicating a mound-shaped structure, and show up as topographic highs in the side-scan phase bathymetry (Figure 3). Their shape is generally a smooth convex-upward hemispherical dome that rarely shows evidence of summit collapse. The nature of the DSL-120 sonar return from the lava mounds limits the size of the features we observe to those that are large enough to have a consistently recognizable mound shape (~20 m base radius), but not so large that their perimeter falls outside the side-scan swath (~500 m base radius). Although lava mounds larger than the DSL-120 were not found along the ridge crest, they would be resolved on multibeam bathymetry if such mounds did exist. A few small pillow constructions (haystacks) are known to exist from near-bottom visual observations but are not included in the same

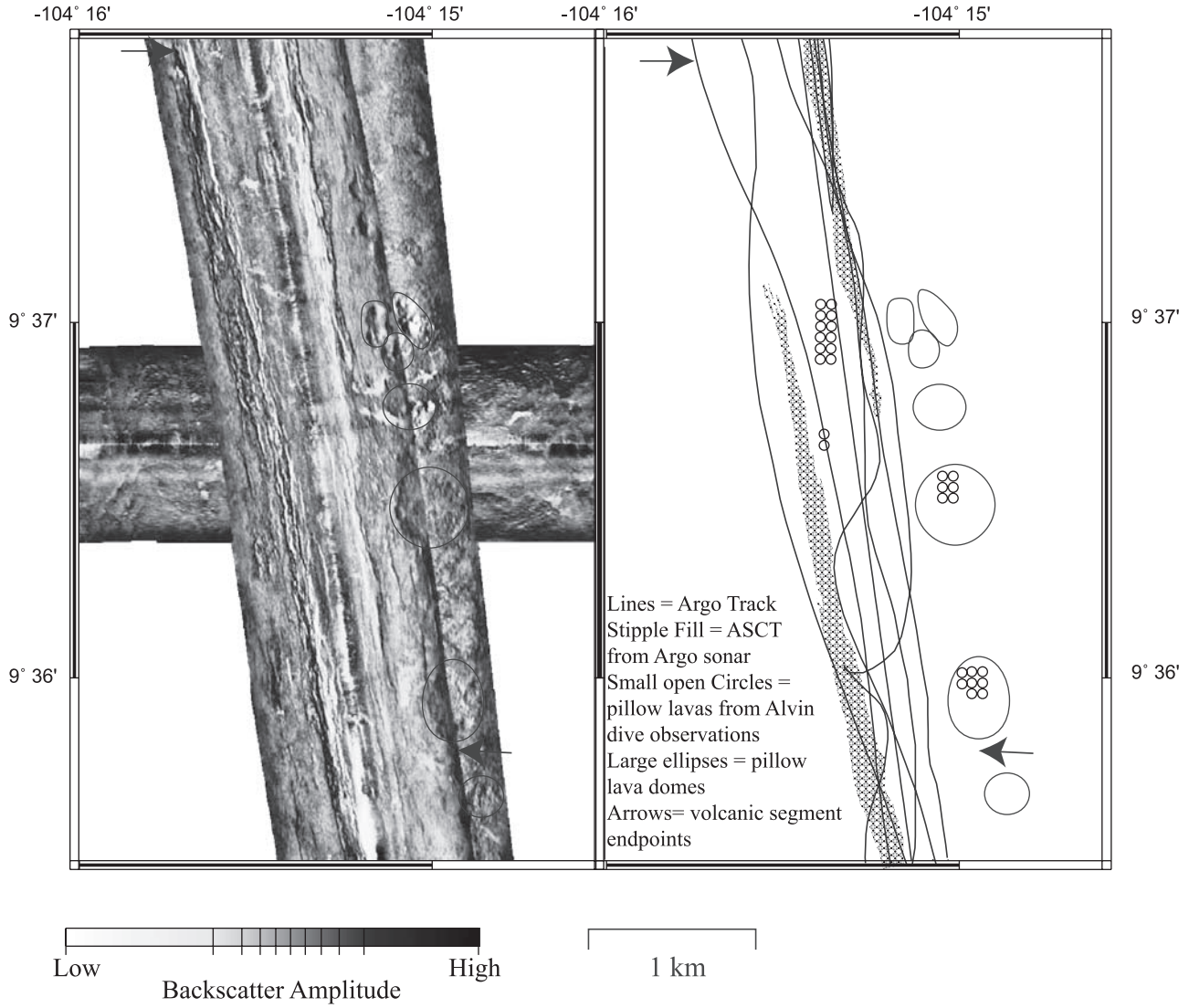

Figure 2. Map of the overlapping axial summit collapse troughs (ASCTs) that form a third-order segment boundary. (left) DSL-120 sonar backscatter imagery. The axial pillow lava domes are circled in black. This area was imaged by two overlapping axis-parallel swaths and one perpendicular swath. (right) The 1989 *Argo* track in bold black lines, the ASCT modified from *Haymon et al.* [1991] in stipple fill, and pillow lavas identified from *Alvin* observations as small circles [*Smith et al.*, 2001]. Axial lava domes form near the segment end and extend to the south of the eastern ASCT limb. Note that most of the pillow lava observations from *Smith et al.* [2001] were outside the 1989 *Argo I* coverage. Pillow domes correspond to locations of pillow lava flows where they have been mapped visually by *Smith et al.* [2001].

category as the larger lava mounds for several reasons. First, haystacks are difficult to identify on DSL-120 records without ground-truth from visual observations. Second, such small edifices may be imaged incompletely, especially in the phase bathymetry, and are difficult to measure accurately. Finally, haystacks and larger lava mounds could result from similar eruptive processes, but haystacks would be volumetrically insignificant in comparison to the lava mounds.

[13] The average radius of the lava mounds in our study area is 128 ± 50 m, and their average height is 20 ± 10 m, within one standard deviation of the mean from their counterparts on the southern EPR, which have an average radius of 100 ± 60 m and average height of 20 ± 10 m [*White et al.*, 2000]. In comparison to the EPR axial lava mounds, the small seamounts on the Mid-Atlantic Ridge are typically larger (~60 m characteristic height) and exhibit a greater range in size [*Smith and Cann*, 1999; *Smith et al.*, 1995]. Pillow mounds found on the Juan de Fuca Ridge and the EPR are similar in size [*Embley and Chadwick*, 1994; *Embley et al.*, 2000].

2.3. Definition of the Axial Zone

[14] Where used herein, the axial zone refers to a 1 km wide corridor centered on the ridge axis where all of the geological features are representative of the present volcanic processes occurring at the ridge crest, and exclude as many of the older, relict features as possible. The 1 km width was chosen to most closely match the width of the axial zone in this study with other studies of active volcanic processes in

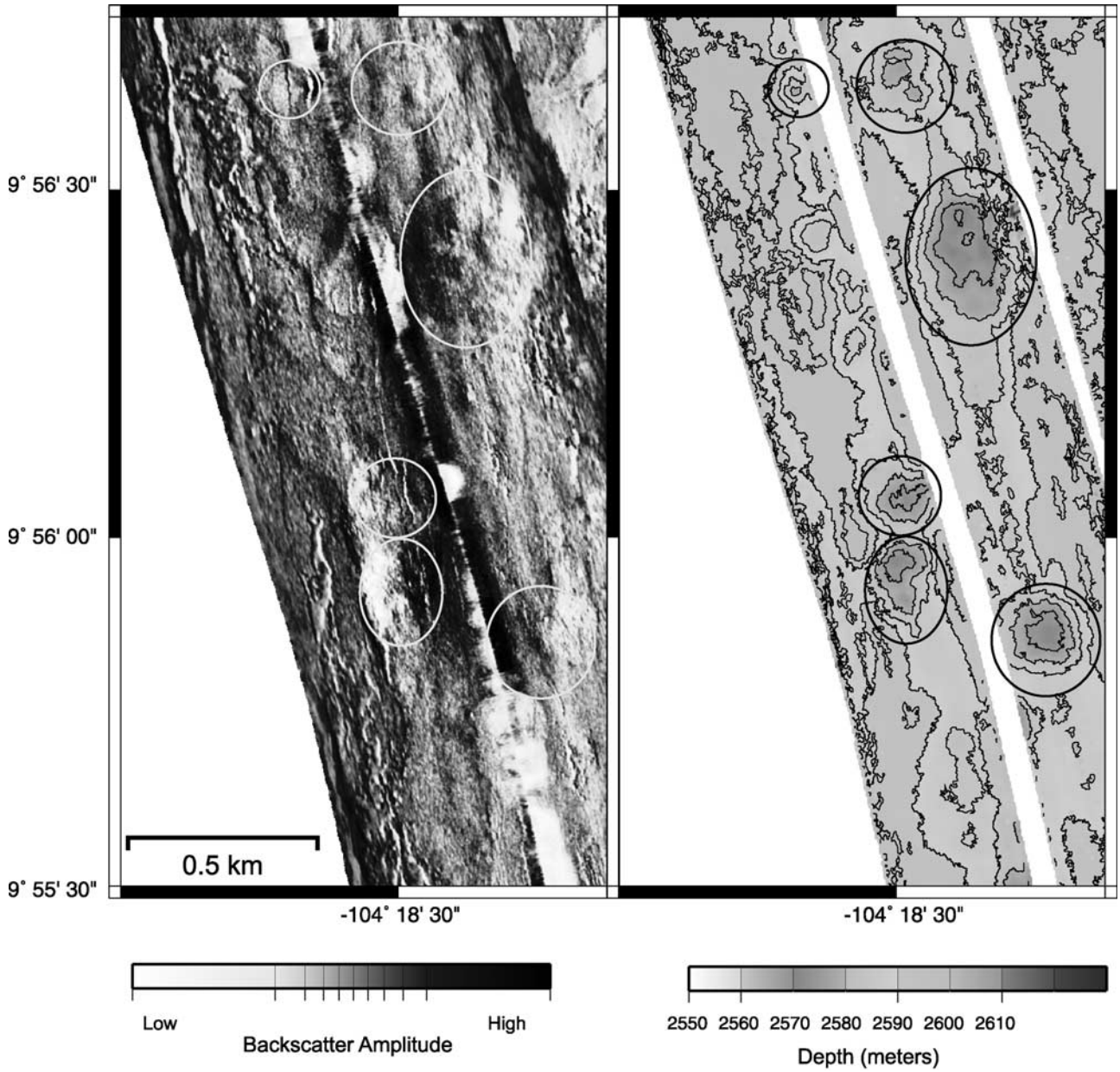

Figure 3. Axial pillow lava domes, circled, found at a third-order segment end. (left) The DSL-120 backscatter imagery. (right) The DSL-120 phase bathymetry contoured at a 5 m interval. Locations of the lava domes are circled. Domes are covered with pillow lava flows where visual observations are available.

this area [*Haymon et al.*, 1993, 1991; *Kurras et al.*, 2000; *Perfit et al.*, 1994; *Smith et al.*, 2001] and on the southern EPR [*White et al.*, 2000]. Additionally, we found lava mounds beyond ~500 m from the ridge axis that appear to be dissected by faults (Figure 4). Faulting suggests that these may be old, inactive structures in the process of being destroyed, and are not representative of current volcanic processes on-axis.

[15] The volcanic structures of interest in this study are those created by axial eruptions of current EPR volcanic systems. Beyond the axial zone, lava flows originating at both the axis and off-axis volcanic constructions are potential sources of pillow lava [*Kurras et al.*, 2000; *Perfit et al.*, 1994]. Volcanic structures may be destroyed by the initiation of normal faulting within a few hundred meters of the ridge axis [*Carbotte and Macdonald*, 1994; *Fornari et al.*, 1998]. All of these factors obscure the pattern of volcanic structures and lava morphology generated by axial eruptive processes. For this reason, we limit our study to within 500 m of the ridge axis where we can be reasonably sure the volcanic morphology reflects the eruptive processes of current EPR volcanic systems.

2.4. Recognition of Axial Pillow Lava Domes

[16] We infer that the pillow mounds formed within the axial zone may be classified as basaltic lava domes. Lava domes differ from lava mounds in that domes have a specific genetic definition, while mounds are any mound-

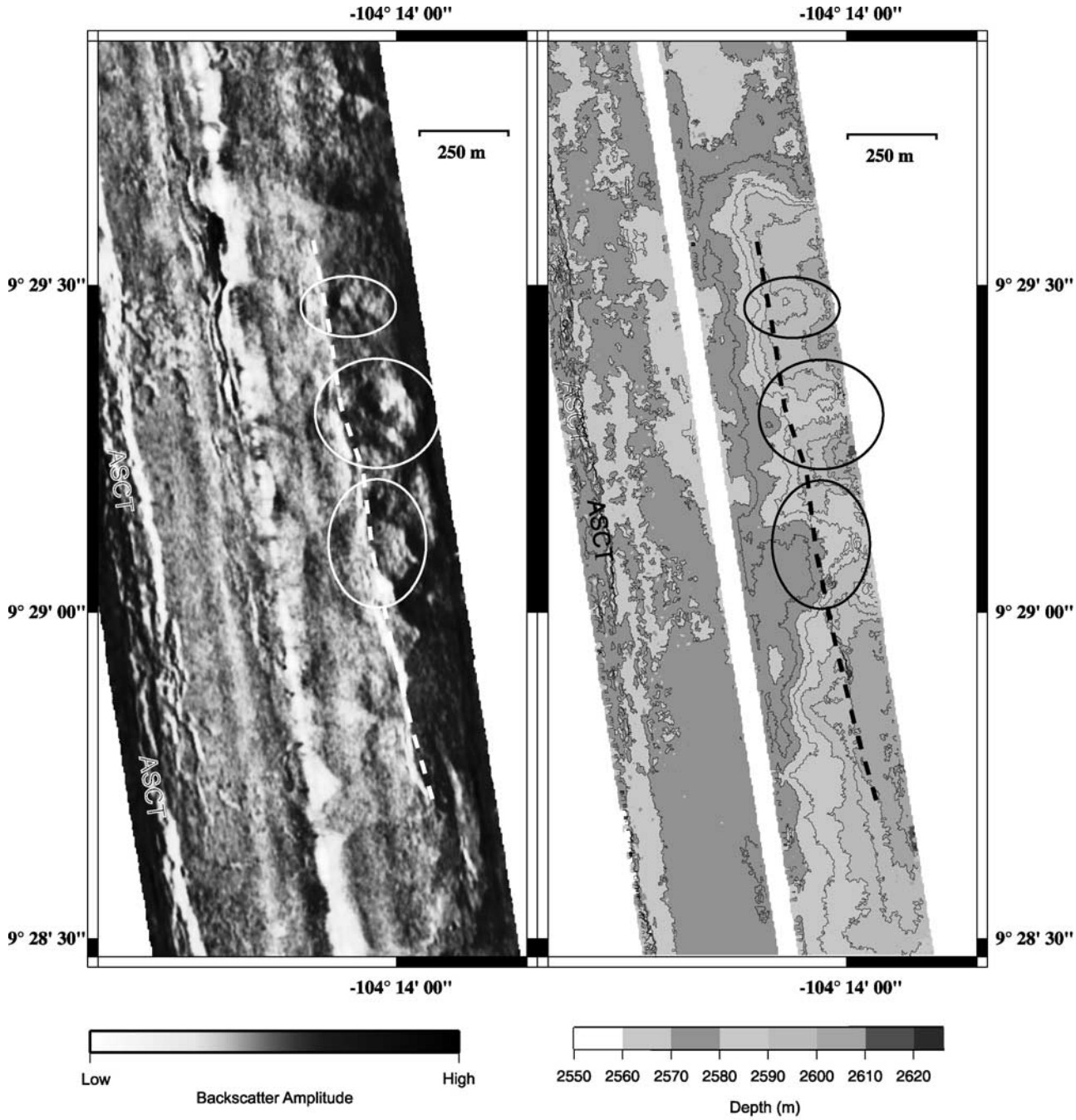

Figure 4. (left) DSL-120 backscatter imagery and (right) phase bathymetry contoured at 5 m interval showing three lava mounds, circled by black lines, that appear to be cut by a fault, indicated by a dashed line. The low-intensity backscatter return (dark) indicates the fault is down-dropped to the east. The ridge axis runs through the axial summit collapse trough seen at the far western edge of the DSL-120 swath.

shaped feature. Lava domes are a steep-sided pile of lava formed by eruption of short lava flows or intrusion into the lava pile over a primary volcanic vent [*Williams*, 1932]. Lava domes are strictly a morphologic classification. In summary, lava domes are defined as (1) relatively steep-sided and round-to-flat topped edifices (2) consisting of short surface lava flows (3) over a primary volcanic vent. The lava domes within our study area meet these criteria that also were used by *White et al.* [2000] to identify pillow lava domes on the southern EPR.

[17] The lava domes in our study area are dominantly composed of pillow lava, and are morphologically similar to lava domes in the axial zone on the southern EPR (Figure 5). Lava domes are found in areas where pillow lava is the locally dominant lava morphology in *Argo I*, *Alvin*, or Woods Hole Oceanographic Institution (WHOI) camera tow images [*Haymon et al.*, 1991; *Smith et al.*, 2001; J. L. Engels et al., Collapse of seafloor volcanic terrain: A key process in the formation of the upper oceanic crust, submitted to *Journal of Geophysical Research*, 2001,

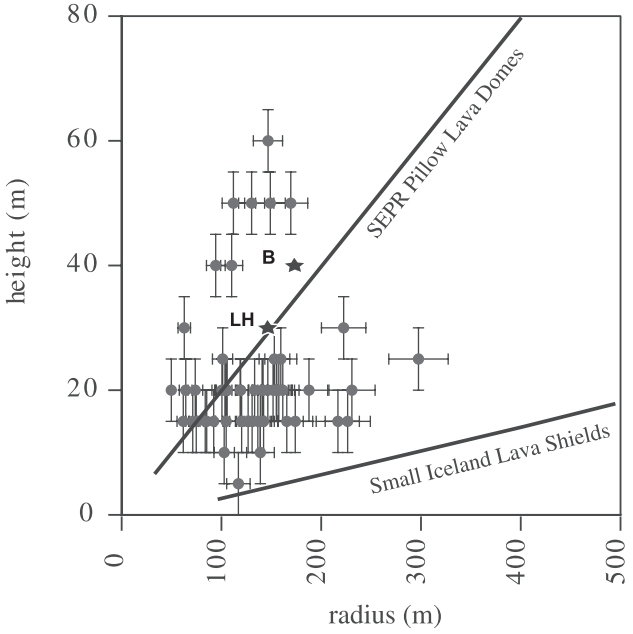

Figure 5. Plot of the height and radius for all pillow mounds within the study area indicating their shape is similar to lava domes. The radius of the dome was calculated as its basal perimeter divided by 2π with error bars showing 10% error based on our ability to measure mound radii by this method. The height error bars indicate 5 m uncertainty. The lines show the least squares linear regression best fit to the height:radius ratio of small Icelandic lava shields ($h = 0.038r$) [*Rossi*, 1996] and basaltic lava domes on the southern East Pacific Rise (SEPR) ($h = 0.2r$) [*White et al.*, 2000]. Two stars show the sizes of small submarine basaltic lava domes (LH) at Low Head-on King George Island [*Smellie et al.*, 1998] and (B) at Bogoslof in the Aleutians [*Miller et al.*, 1998]. The NEPR pillow constructions are too small and steep to be classified as lava shields but are very similar to other documented small basaltic lava domes.

hereinafter referred to as Engels et al., submitted manuscript, 2001]. Pillow lava flows spread slowly, causing lava to pile up around its eruptive vent thus forming lava domes [*Gregg and Fink*, 1995; *Griffiths and Fink*, 1992]. The ridge crest within our study area has a regional along-strike gradient of ~1 m/km making it highly unlikely that lava could be transported along-strike by gravitationally driven flow through lava tubes and form ~20 m high mounds. Further, the lava domes appear to be independent lava flow units from observations of sediment cover and crosscutting relationships, rather than part of one long lava flow as expected for secondary volcanic edifices. The classification of lava domes may only apply to those lava mounds found within the 1 km wide axial zone, because seafloor slope is often considerably higher on the ridge flanks.

2.5. Volcanic Structures and Third-Order Segments

[18] Third-order segment boundaries identified in multibeam bathymetry correspond to locations where pillow lava domes and breaks in the continuity of the ASCT occur. It is significant that both gaps between ASCT segments, the fissure-cut relay zone from 9°43.5′N to 9°45′N and the overlapping ASCT segments around 9°37′N, correspond to third-order segment boundaries identified in the multibeam bathymetry. Where the ASCT is continuous, no segment boundaries are found.

[19] Pillow lava domes are found near four out of five third-order segment boundaries identified from multibeam bathymetry (Figure 6). When lava domes within only 250 m of the axis are considered instead of those within the full width of the axial zone, a smaller total number of lava domes are still associated with four of five segment ends. This implies that our result is not uniquely produced by the particular width defined for the axial zone.

[20] The absence of any lava domes at the third-order segment boundary at 9°45′N merits further comment. This offset of the ridge axis is apparent in multibeam bathymetry and is a prominent structural discontinuity in the ASCT in the DSL-120 records as well (Figure 7). The axial zone exhibits a swarm of fissures in older terrain at the southern edge of an area that experienced an eruption in 1991 [*Haymon et al.*, 1993]. Although no lava domes occur, pillow lavas are relatively abundant in the *Argo I* data, and create small pillow haystacks. The exact position of the third-order segment boundary is less distinct than any of the others in this study. Perhaps it is just developing, or is being overprinted. As *Macdonald et al.* [1988] point out, segmentation of oceanic ridges is a continuum, and not all segment boundaries will fit easily into one classification.

[21] The absence of lava domes at 9°45′N highlights an interesting difference between volcanic structures on the

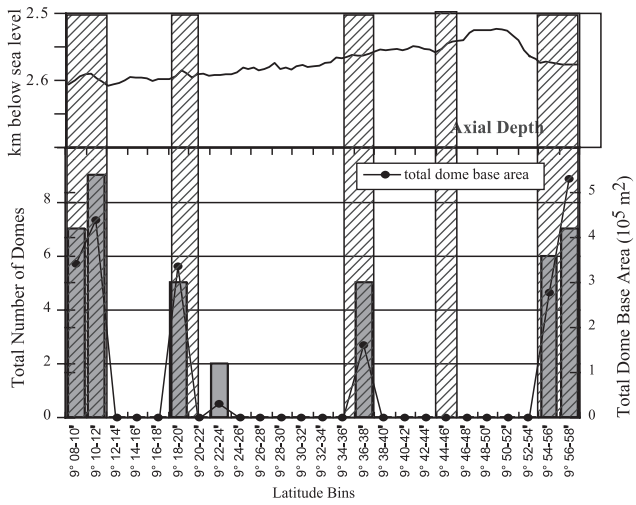

Figure 6. (top) Ridge axis depth within our study area shown at nearly 100X vertical exaggeration, with a small (<100 m) depth variation. (bottom) The abundance of pillow lava domes in the axial zone (<500 m from the ridge axis) plotted by latitude in 2′ (~4 km) bins. Total number of domes is shown by vertical columns, and the total basal area of the lava domes is shown by black dots. The areas where most lava domes are located correspond very well to bins where the third-order segment ends are located (shown by hashed lines). Comparison of axial depth to the presence of lava domes illustrates that depth variations do not define third-order segment boundaries or the determine the locations of lava domes.

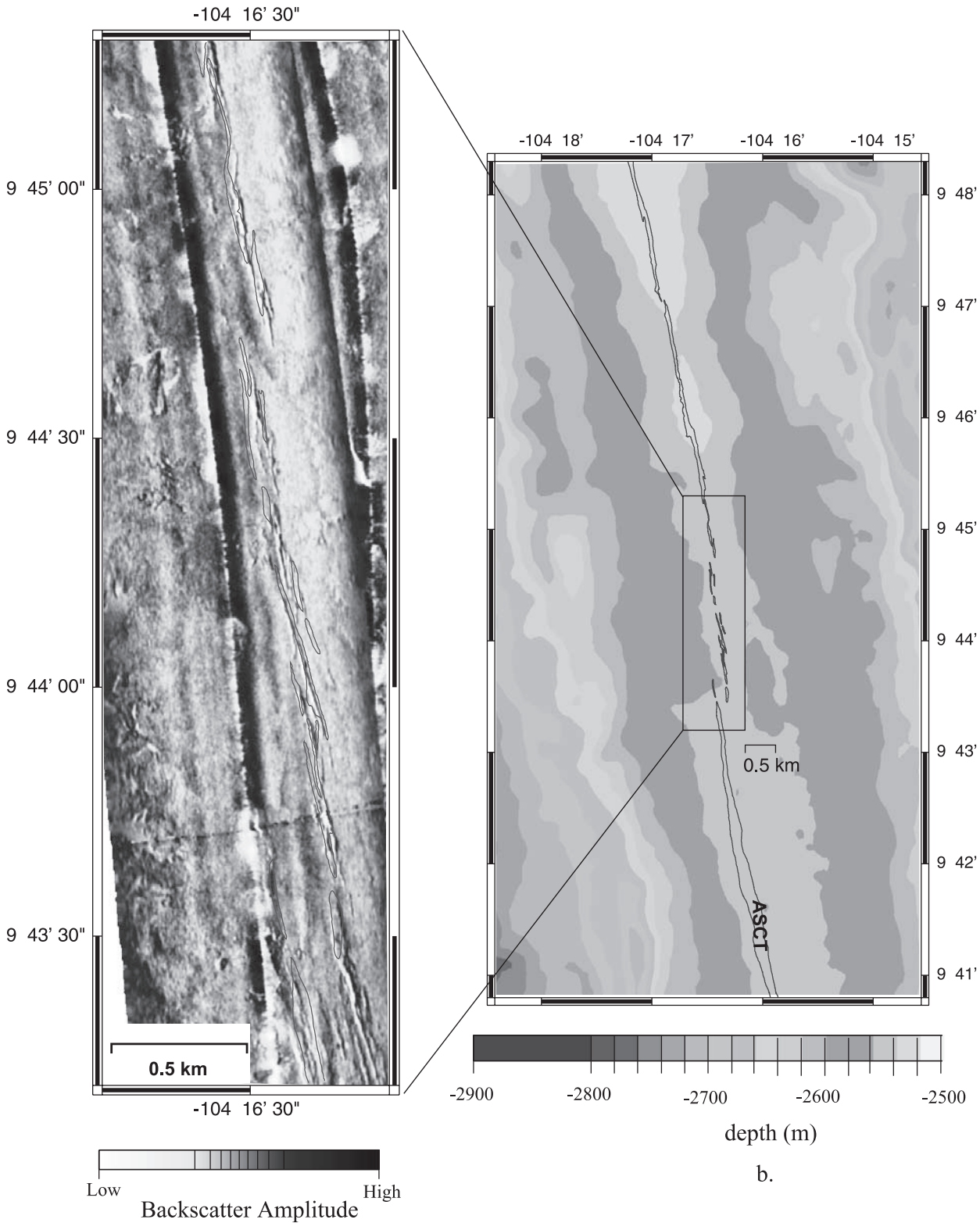

Figure 7. The atypical third-order segment boundary zone at 9°44.8′N has widespread areas of small collapse pits unusual for third-order segment boundaries, although a high abundance of pillow lava is found here. (a) The DSL-120 backscatter imagery showing the en echelon fissures that form a relay zone between two axial collapse troughs. The ridge axis steps right a total of 500 m through this fissure zone. The paired light-dark reflectors are fissures. (b) The Sea Beam 2000 bathymetry [*Cochran et al.*, 1999] with a 10 m color change interval on the axial high, illustrating the right-lateral offset and a pinching of the width of the axial high at this ridge discontinuity.

Table 2. Visual Coverage of the *Argo* Survey Track Lines Within a Corridor of Specified Width About the Ridge Axis[a]

Maximum Distance From Ridge Axis in Corridor, m	Seafloor Imaged,[b] %	Area of Seafloor Imaged, km^2
100	34	2.58
250	23	4.30
500	14	5.50

[a] Coverage within 500 m was used to determine the lava morphology in this study.
[b] As percent of total seafloor within corridor.

EPR at 9°–10°N and those at 17°–18.5°S. Pillow lava domes are rare at 9°–10°N, and located exclusively at segment ends; whereas lava domes at 17°–18.5°S are found all along the ridge but occur much more abundantly at segment ends. In contrast, the collapse troughs forming the ASCT are quite extensive at 9°–10°N, covering most of the length of three third-order segments, whereas the collapse troughs at 17°–18.5°S are much smaller and cover only ~25% of the total third-order segment length of two segments out of eight. However, all of these ASCT structures probably result from extensive lava carapace collapse [*Fornari et al.*, 1998]. While it is clear that the eruption history of the EPR at 9°–10°N is different from that at 17°–18.5°S, the overall distribution of volcanic structures with respect to third-order segmentation is similar.

3. Lava Flow Morphology

3.1. Data Acquisition and Analysis

[22] Visual observations of lava flow morphology in the axial zone of the EPR from 9°09′ to 9°55′N were obtained in November 1989 using multiple camera systems on *Argo I* [*Haymon et al.*, 1991]. The axial zone was surveyed in long, axis-parallel lines from 9°08′ to 9°54′N. *Argo I* was towed 7–10 m above the bottom, resulting in a 10–16 m visual swath width [*Wright et al.*, 1995]. For this study, we use several long, axis-parallel *Argo I* track lines spaced 10–50 m apart. This set of track lines provides dense visual coverage within the ASCT but the coverage density decreases with distance from the ridge axis (Table 2). *Haymon et al.* [1991] describe the *Argo I* survey logistics in detail. Lava flow morphology data was tabulated during the 1989 survey, but not quantitatively analyzed until now.

[23] We have compiled the real-time lava morphology data from the 1989 *Argo I* survey, reclassifying the detailed original observations into three categories: sheet, lobate, and pillow lava flows. Sheet lava flows included all smooth, ropy, or hackly lava flows logged during the *Argo I* survey. Sheet flows are characterized by flat surfaces with either a broken or smooth crust. Lobate lava flows remain unchanged from the real-time *Argo I* classification scheme. Lobate flows have rounded to bulbous surfaces with a smooth crust. Pillow lava flows include both bulbous and tubular pillows logged during the *Argo I* survey. Pillows have well-rounded surfaces with a distinctive striated and cracked crust. Examples illustrating the variations in appearance used to classify lava morphology from this area are presented by *Kurras et al.* [2000].

[24] Lava morphology observations logged in real time were spot-checked against photographs taken at the same time during the *Argo I* survey to ensure that the logged observations were accurate records of the lava morphology. For another check of the accuracy of the real-time observations, the lava morphology at points where the *Argo I* lines crossed was checked in a geographic information system database to see if both observations were the same. We found that in most cases, the observations were in agreement suggesting a high level of internal consistency in the data.

[25] To determine the spatial distribution of lava morphology, we applied the conversion of point observations to areas used by *White et al.* [2000] for *Argo* II data on the southern EPR by modifying the procedure described by *Wright et al.* [1995] for mapping lava age distributions. The *Argo I* observations were made at random intervals, usually after crossing a lava morphology contact, and logged at a specific time. Thus, the lava morphology observation data consist of points in space defined by the position of *Argo I* when the observations were made. Because these points actually represent areas, the number of observations of a given lava morphology has no intrinsic meaning and must be adjusted by the area that the observation represents. To do this, the original point observations are expanded into areas where the size of the area corresponds to the spacing between the data points by the point-in-polygon method. This point-to-area conversion works well for statistical comparisons of regions, but it can result in some repositioning of contacts, thus making it unsuitable for making geologic maps of specific areas. To compare the variability of lava morphology to third-order segmentation, we require a statistical quantification of lava morphology within ~20 km long segments rather than a precise map of an area, so this method is adequate for our purposes.

[26] To determine the variation in lava morphology within the third-order segments, we bin the data by latitude along the axial zone to examine the variation displayed over each volcanic system independently. Because the volcanic systems are 15–30 km long, we chose a 2′ (~4 km) bin interval as the optimal length to have enough bins to emphasize regional trends, while minimizing noise in the data.

3.2. Observations

[27] Low-effusion rate pillow flows and high-effusion rate sheet flows are anticorrelated by latitude, an initial indication that the distribution of lava morphology has a large-scale organization. By latitude, pillow and sheet lava flow morphology show more variation in relative abundance overall than lobate lava flows (Figure 8). The relative abundance of pillow compared to sheet lava flows is closely related to the third-order segments. Pillow flows are limited to ends of the ASCT segments, and are otherwise completely absent within the ASCT. In contrast, the abundance of lobate lava flows varies surprisingly little in the study area.

[28] The pillow lava abundance reaches local maxima near each of the third-order segment ends (Figure 8). Abundant pillow lava corresponds to pillow lava domes in most locations. However, the 9°44.8′N third-order segment boundary has a prominent local maximum in pillow abundance that is unrelated to formation of pillow lava domes. In this instance, the distribution of lava morphology indicates the trend toward decreased lava effusion rate in the absence of recognizable pillow lava domes.

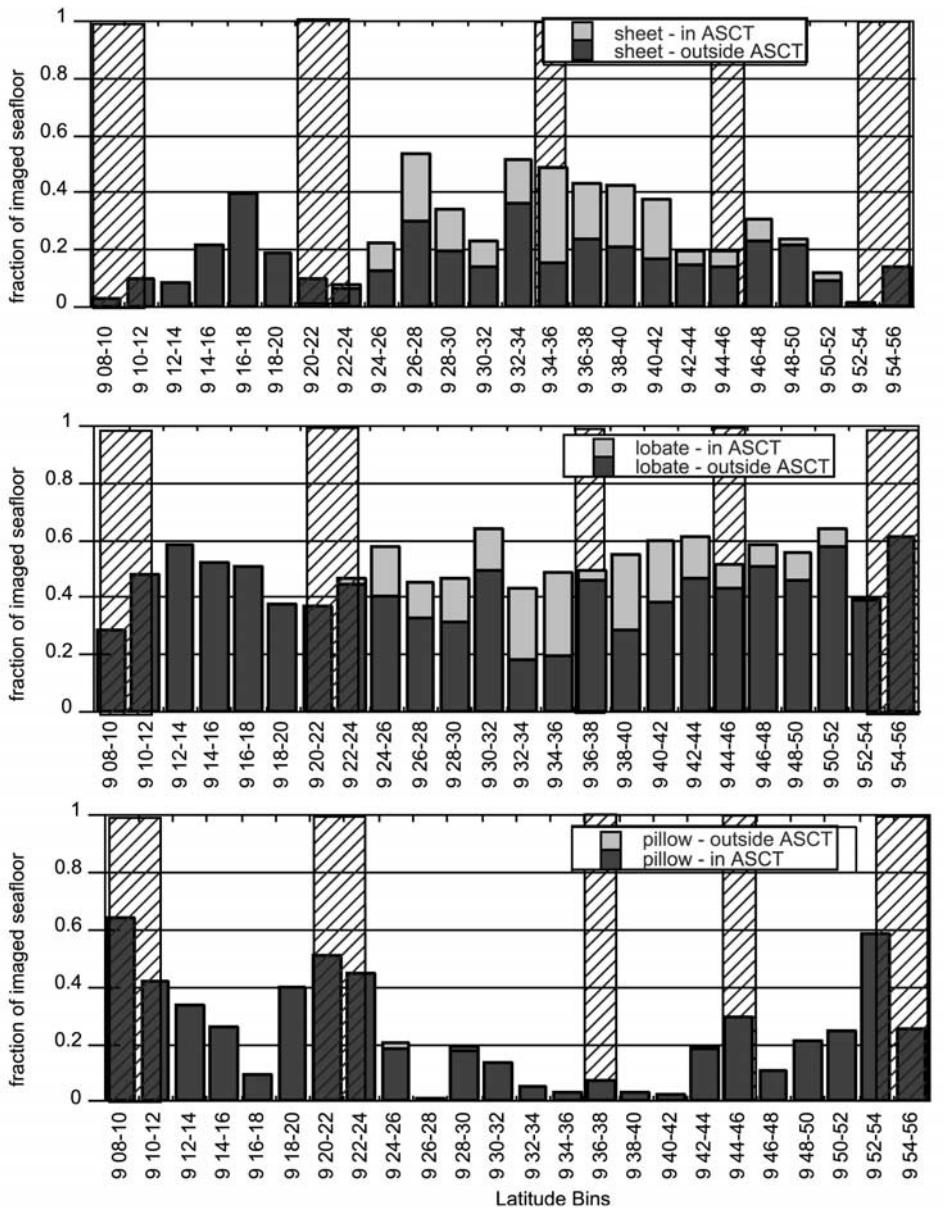

Figure 8. Histogram plot of the lava morphology distribution from *Argo* observations in 1989 along the axial zone (<500 m from the ridge axis) plotted in 2′ (∼4 km) latitude bins. The relative abundance of each flow morphology is shown as a fraction of the seafloor imaged in the *Argo* survey for each bin, so that all three panels will sum to 1. Darker fill in the columns indicates observations outside the axial summit collapse trough (ASCT), while lighter fill indicates observations made within the ASCT. Almost no pillow lava was found within the ASCT. Hashed lines indicate third-order (volcanic segment) discontinuity zones shown in Figure 1. All third-order discontinuities correspond to local maxima in the relative abundance of pillow lava, but sheet flows are most abundant near midsegment.

[29] Observations by latitude may be affected by the locations of the *Argo I* track lines. For example, the segment boundary at 9°36′–38′N was surveyed by towing *Argo I* up one ASCT limb, then angling across the overlap zone to the next ASCT, so that the segment ends were missed (Figure 2). As a result, this area appears to have a lower percentage of pillow lava than it would show if coverage were extended to the segment ends [*Smith et al.*, 2001; Engels et al., submitted manuscript, 2001]. Even so, this area still shows a small local increase in the abundance of pillow lava relative to the surrounding areas (Figure 8). Checking the *Argo I* tracks against the DSL-120 records, we believe that *Argo I* coverage was sufficiently extensive that a representative sampling of lava morphology was obtained.

[30] Overall patterns in lava morphology in our study area exhibit some differences from the distribution noted in earlier work on fast spreading ridges that relied on more limited camera-tow or submersible observations [*Auzende et al.*, 1996; *Gente et al.*, 1986; *Kurras et al.*, 2000; *McConachy et al.*, 1986; *Renard et al.*, 1985]. Of the total area

visually imaged by *Argo I*, approximately 25% is pillow lava, 50% is lobate lava, and 25% is sheet lava. Fast spreading ridges had been thought to erupt primarily (~80–90%) sheet flows in the neovolcanic zone [*Bonatti and Harrison*, 1988; *Perfit and Chadwick*, 1998]. This is not the case although sheet and lobate flows together do cover most of the axial zone. Pillow flows are nearly twice as abundant as previously estimated.

[31] Sheet flows show an abundance pattern related to the ASCT in addition to a correlation with the centers of third-order segments. Sheet flows are more abundant in the third-order segments where an ASCT is present. Sheet flows generally cover 25–50% of the total area imaged by *Argo I* in and surrounding the ASCT between 9°23′ and 9°52′N (Figure 8). Otherwise, sheet flows generally cover less than 10% of the total area imaged by *Argo I* in areas without an ASCT. This is similar to the lava morphology distribution on the southern EPR, where sheet lava flows were sparse (<10% of total imaged seafloor) except in the region surrounding Aldo Lake trough [*White et al.*, 2000].

4. Relationship Between Lava Morphology and Volcanic Structure in Axial Zone

[32] To quantify the relationship of third-order segmentation to volcanic features for all of the segments in the study area, the number of lava domes and the relative abundance of each lava morphology, respectively, are stacked to obtain a cumulative distribution with respect to location within the third-order segments. Individual volcanic segments are likely to be in different stages of volcanic activity at any particular time. For example, even though pillow lava domes tend to occur near segment ends most of the time, any given segment at any particular time might have a sheet flow covering significant parts of the segment end (e.g., Engels et al., submitted manuscript, 2001). To reduce the effects of temporal variation, we stack all four complete third-order segments in our study area together.

[33] To account for segments of different lengths, we used a percentage distance calculated from the centroid of each lava dome base to the segment end, divided by half the total segment length. The same procedure was used for lava morphology, except that the area of each lava morphology had to be divided into discrete blocks of arbitrary size, based on a subdivision of the point-to-area conversion, so that the distance of each block from the segment end can be measured. This calculation gives the percent distance from the segment end as a method of normalizing for segments of different lengths. The data were divided into five bins along-axis, each representing 20% of the total segment length. The five bins are enough data points to define a trend while minimizing errors due to small numbers of observations or unequal survey coverage.

[34] Both the abundance and total base area of lava domes decrease dramatically from segment end to segment center when normalized to segment length and stacked (Figure 9a). In fact, over half the total area covered by lava domes lies within the 20% of the area closest to a segment end, and no lava domes are found in the middle 40% of the segments. Note that this calculation only uses the four segments where we have complete DSL-120 coverage; in addition, ten more lava domes are actually observed in the DSL-120 data near third-order segment ends that are not included in Figure 9a.

[35] When the lava morphology data from all four complete segments in the study area are stacked and normalized to segment length, the relative abundance of pillow lava flows decreases with distance away from third-order segment ends (Figure 9b). Sheet lava flows show the opposite relationship: an increase with distance away from third-order segment ends (Figure 9b). The abundance of lobate lava flows shows very little variation within third-order segments, indicating that local eruption processes are dominated by conditions that will produce lobate lava flows.

[36] Lava morphology data along third-order segments indicate systematic trends in the kilometer-scale distribution of lava flows, instead of a random distribution. Variations in the lava effusion rate, slope of the pre-existing seafloor, or lava viscosity may be causing random changes in lava morphology on small scale (<100 m), but this random meter-scale variability in individual lava flows occurs within a more organized overall distribution of lava morphology revealed by along-strike *Argo I* mapping over several kilometers. The anticorrelation of pillow and sheet lava flows (Figure 9) acts as the critical discriminator in the study area, and suggests that eruptions at one location tend to produce either pillow or sheet lava flows along with lobates over time.

[37] The lava morphology corresponds closely to the type of volcanic structures on the ridge axis. Flat lobate and sheet flows are the most likely to create thin-crusted lava ponds with numerous lava pillars [*Gregg and Chadwick*, 1996]. Our observations of lava morphology show that sheet flows are most common in the ASCT (Figure 8). In contrast, a lava dome forms when lava piles up around an eruptive vent; lava domes and pillows can indicate either lower effusion rates or higher lava viscosity. Our observations of lava morphology show that, overall, pillow lava flows are most abundant in the places where the basaltic lava domes form. The formation of pillow domes only near third-order segment ends suggests the eruptive style within third-order segment boundary zones is significantly different than near segment centers.

[38] What if the axial pillow lava domes were actually secondary (rootless) volcanic edifices and not true lava domes at all? If the putative lava domes are actually secondary edifices, it would not affect our interpretation of organization of volcanic systems along the ridge. In fact, it would imply that most eruptions occur near the middles of segments, requiring an even more focused magma supply than our preferred interpretation of the pillow mounds forming as true lava domes within the axial zone.

5. Correlative Evidence for Volcanic Segmentation

[39] The tendency for pillow lava and basaltic lava domes to form near third-order segment ends suggests that magma delivery to the eruptive vents near segment ends is disrupted or less efficient. If disruptions to the magma delivery system are characteristic of volcanic segmentation, then these disruptions may also be manifested in the chemistry of the lava, the structure of the crust, and the geometry of magma reservoirs. Therefore, we examine results of numerous studies of crustal structure and composition on the EPR at

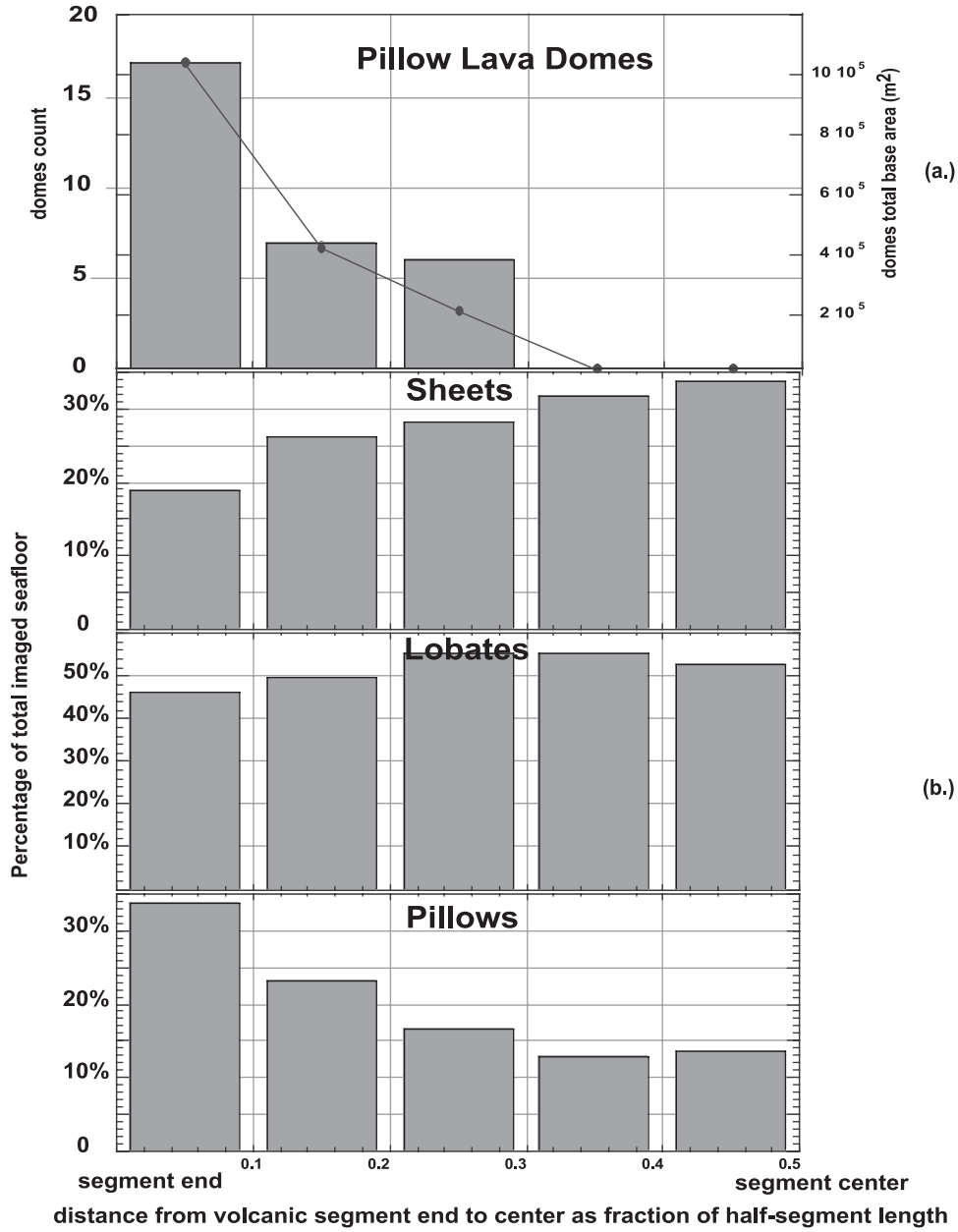

Figure 9. Histogram of (a) total number of pillow lava domes and (b) relative abundance of each class of lava morphology in the axial zone for all segments combined. Bin interval is normalized to 20% of the distance from the end to center of each segment in order to adjust for varying segment length. Total basal area of the lava domes in each bin is shown as black dots connected by lines. Pillow lava domes are most abundant and cover a greater area of seafloor near the segment ends in the bin at the third-order segment end. Lobate lava flows are consistently more abundant than either pillow or sheet lava flows alone. Pillow lava is more than twice as abundant at the segment end as it is near segment centers, and sheet lava flows have the reverse relationship to segmentation. From this, we infer that lower eruption effusion rates are more typical of eruptions near the ends of third-order segments, producing the pillow lava domes there. These data provide one line of evidence that the third-order segments correspond to individual volcanic systems along the EPR.

9°–10°N to see if these datasets are consistent with volcanic segmentation at third-order discontinuities.

5.1. Seismic Imaging of the Axial Magma Chamber

[40] Seismic reflection profiles of the EPR at 9°–10°N show prominent axial magma chamber (AMC) reflectors ~1500 m below the seafloor under most of the ridge axis [*Detrick et al.*, 1987]. Eight seismic profiles perpendicular to the ridge and a three-dimensional (3-D) tomographic study provide additional constraint on subsurface structure [*Dunn et al.*, 2000; *Kent et al.*, 1993a, 1993b; *Toomey et al.*, 1994]. Spatial correlation between segmentation of the

AMC and third-order segmentation would provide evidence that third-order segments are separate volcanic systems [*Sinton and Detrick*, 1992]. Gaps between volcanic systems may correspond to changes in the depth and width of the AMC imaged in seismic reflection profiles. However, large changes in the melt:crystal ratio in the AMC are found even where the AMC is apparently continuous along strike [*Singh et al.*, 1998]. Thus the segmentation of the AMC to along axis magmatic flow may be indicated by subtle changes in its seismic characteristics.

[41] Each of the third-order segment boundaries corresponds with some type of discontinuity in the AMC (Table 1). A break in the AMC reflector is noted in the 9°57′N third-order segment boundary zone [*Detrick et al.*, 1987; *Vera and Diebold*, 1994]. The depth to the AMC increases and the width decreases by ~200 m at 9°45′N compared to the next closest ridge-perpendicular seismic profile to the south [*Kent et al.*, 1993a]. Seismic imaging indicates that a pinch-out of the AMC occurs at the segment boundary centered at 9°37′N [*Kent et al.*, 1993a; *Toomey et al.*, 1994]. At the 9°20′N segment boundary, *Kent et al.* [1993a] infer a right-lateral jump of the AMC associated with an increase in AMC width. Another break in the AMC reflector was found in the 9°10′–12′N third-order segment boundary zone [*Detrick et al.*, 1987; *Kent et al.*, 1993b].

[42] Only one seismic discontinuity has been proposed that fails to correspond to the third-order segment discontinuities: an anomalous high seismic velocity at 9°28′N near the depth of the AMC [*Dunn et al.*, 2000; *Toomey et al.*, 1994]. The nature of this discontinuity is equivocal, because it is only seen in the seismic tomography data as a small velocity increase near the edge of the tomographic survey box and is not apparent at the depths where the AMC should be present [*Dunn et al.*, 2000; *Toomey et al.*, 1994]. Further, no discontinuity appears at 9°28′N in the seismic reflection profile of the AMC [*Detrick et al.*, 1987; *Kent et al.*, 1993a] or in seafloor morphology [this study; *Haymon et al.*, 1991]. Otherwise, all third-order ridge discontinuities identified from the ridge morphology match the locations of disruptions to the AMC indicated by seismic studies.

5.2. Geochemical Variations

[43] The geochemical composition of axial basalt has been shown to correlate with ridge-crest segmentation, and has been related to the organization of magmatic plumbing systems. Initial results from along axis dredging (>5 km spacing) between 9°17′N and 9°51′N suggested geochemical discontinuities consistent with morphological discontinuities located at ~9°20′N, and ~9°53′N [*Langmuir et al.*, 1986]. Additional sampling at ~2 km spacing produced results consistent with either a single, narrow, chemically zoned magma chamber beneath the ridge in this region, or a single geochemical discontinuity at 9°37′N [*Batiza and Niu*, 1992]. However, volcanic segment (third-order) discontinuity zones that we have identified span only ~3 km along-axis, so sample spacing on a much finer scale than this is necessary to resolve the segmentation. Dense sampling (10–500 m spacing) in the axial zone from 9°28′N to 9°56′N using *Alvin* [*Perfit and Chadwick*, 1998; *Perfit et al.*, 1994; *Smith et al.*, 2001] provides an adequate sample spacing to resolve the volcanic segment discontinuity zones.

[44] Geochemical discontinuities are typically expressed as significant changes in lava composition, differences in incompatible element ratios or isotopes, or great variability in lava chemistry [e.g., *Batiza and Niu*, 1992; *Langmuir et al.*, 1986; *Perfit et al.*, 1994; *Smith et al.*, 2001; *Sims et al.*, 2002]. Extremely variable lava composition with similar isotopic trace element source characteristics may indicate changes in-depth of melting or inefficient magma plumbing systems from a uniform mantle source [*Sims et al.*, 2002]. Such changes in magma generation and transport would be expected at the ends of a volcanic segment. Compositional variability might not be surprising in light of the complex geology we observe in the volcanic segment boundary zones where pillow and lobate flows often interfinger or may even be overprinted by the occasional lava channel. However, significant chemical variations among lava flows over a small area illustrate why multiple well-located samples are needed to establish the range of variability of lava compositions at volcanic segment boundaries. Rock samples collected from *Alvin* dives provide the type of closely spaced and well-located samples necessary to discern the geochemical characteristics of a volcanic system at the scale of third-order segments. For example, *Smith et al.* [2001] document a geochemical discontinuity in lava composition and hydrothermal fluid chemistry associated with the ~500 m wide discontinuity at 9°37′N. The range of axial basalt compositions within the bounds of the 9°37′N discontinuity zone is strikingly large, being nearly as great as it is along the entire second-order segment from 9°03′N to 10°N. *Smith et al.* [2001] also suggest the eruption of enriched mid-ocean ridge basalt (E-MORB) and evolved normal MORB (N-MORB) at the dying limb of the OSC is a consequence of it marking the end of a volcanic segment.

[45] The extensive suite of samples from 9°30′–56′N collected with *Alvin* allows us to examine the geochemistry across three third-order segment boundaries. For the purposes of this study, we restrict our comparison to Mg # ($Mg/Mg + Fe^{2+}$) [*Perfit et al.*, 1994; *Smith et al.*, 2001]. Mg # generally indicates how evolved a particular lava is, and can be used as a proxy for magma temperature. Lava with an Mg # in the 65–70 range is considered relatively primitive, whereas lower numbers reflect an increasing extent of fractional crystallization and cooler magma temperatures. Crystal fractionation is enhanced in smaller, cooler, or more poorly mixed magma reservoirs, such as those expected at volcanic segment boundaries where the storage and plumbing systems are likely to be less continuous. Decrease in Mg # with decreasing latitude south of 9°50′N was previously ascribed to decreasing temperatures due to thermal and chemical zonation of a single central magma chamber [*Batiza and Niu*, 1992]. However, the range of Mg # at the 9°37′N discontinuity nearly encompasses the entire range along axis. Recent work by *Sims et al.* [2002] indicates that the depth of melting can influence primitive Mg # suggesting that magma genesis, rather than storage, controls these trends.

[46] Because we are looking for what may be small disruptions in the magmatic system, the minimum Mg # sample is used to indicate where the most fractionated lava erupts (Figure 10). Within each of the two well-sampled segments, the samples with lowest Mg # are found closest to the segment ends. Also, the samples with the highest

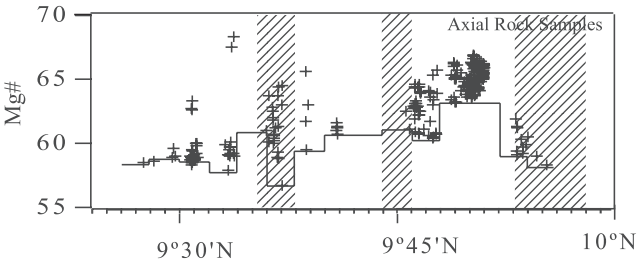

Figure 10. Comparison of third-order segmentation to Mg # of basalt glass samples from microprobe analysis on rock samples collected in our study area by *Alvin* [*Perfit and Chadwick*, 1998; *Smith et al.*, 2001]. The line is a step function showing the minimum Mg # every 3.7 km (2′) along axis, the same bin interval used for the histograms in Figures 6 and 8. Hashed lines mark the third-order segment discontinuity zones (from Figure 1). Within third-order segments the minimum Mg # values are found in the discontinuity zones. Also, there is more chemical heterogeneity in lava near segment ends. This is consistent with the morphostructural and seismic data suggesting that volcanic systems are disrupted at third-order discontinuities.

minimum Mg # are found at the centers of the third-order segments, although the samples with maximum Mg # values do not necessarily occur there (Figure 10). Where we do have a dense grid of well-located rock samples, we conclude that the most fractionated lava does correspond with third-order segment ends. Further work in this area is needed to establish the relationship between the lava geochemistry and third-order segmentation.

6. Discussion

6.1. Volcanic Segmentation: How Does It Differ From Fourth-Order Segmentation?

[47] The correlation of morphostructural, seismic, and geochemical discontinuities indicates that third-order segmentation of volcanic systems affects the entire crustal section. In contrast, fourth-order segments originally were defined as morphologically distinct segments created by eruptive fissures that could change with each new eruptive episode [*Haymon et al.*, 1991; *Macdonald et al.*, 1988]. On the basis of much finer-scale seafloor mapping, *Haymon* [1996] predicted that the hydrothermal systems are controlled at the fourth-order scale by individual dike injections or eruptions. These predictions were largely corroborated by time series studies of the hydrothermal vents on the northern EPR (NEPR) that found compositional changes in the hydrothermal vent fluid were influenced by a single eruption [*Von Damm*, 2000; *Von Damm et al.*, 1995]. Hydrothermal systems are also sensitive to the structure of the volcanic carapace such that the widest fissures, especially those associated with the ASCT, tend to become preferential conduits for hydrothermal flow [*Wright et al.*, 1995].

[48] Each new episode of dike injection and eruption on the EPR has the potential to reorganize hydrothermal circulation by changing the thermal properties and permeability of the upper crust within existing third-order segments. Dike injection appears to be centralized at one location on some third-order segments (e.g., 9°10.4′–21′N/fourth-order segment G) or distributed into several segments on others (e.g., 9°19′–37.9′N/fourth-order segments D, E, and F) (Figure 1) [*Haymon et al.*, 1991]. Some volcanic segments may change their position or geometry over time by propagating along axis leaving faint bathymetric and magnetic migration traces [*Cormier et al.*, 1996; *Lee et al.*, 1996; *Smith et al.*, 2001]. Otherwise, we infer that only large magmatic events would cut through and reorganize volcanic segments. In either case, estimates for the longevity of volcanic segments ($\sim 10^4$–10^5 years) are 1–3 orders of magnitude higher than for fourth-order segments ($\sim 10^2$–10^3 years) [*Macdonald et al.*, 1992; *White et al.*, 2000]. Therefore the present pattern of hydrothermal segmentation may reorganize tens or hundreds of times while volcanic segmentation remains fairly stable.

6.2. Causes of Lava Flow Morphology Variation Within Volcanic Segments

[49] The abundance of pillow lava at third-order segment ends and the sheet-flow dominated at segment centers in our NEPR study area resembles segment-scale lava morphology variations observed on the SEPR [*White et al.*, 2000] as well as the Juan de Fuca Ridge [*Embley and Chadwick*, 1994; *Embley et al.*, 2000]. The causes of lava flow morphology variation may provide insight on volcanic processes at fast spreading ridges generally. Four factors are thought to exert control on lava flow morphology in the submarine setting: lava cooling rate, the slope over which the lava travels, lava viscosity, and lava effusion rate [*Griffiths and Fink*, 1992]. We evaluate each of these factors in the context of the NEPR as a possible cause of lava flow morphology variation within volcanic segments.

[50] The lava cooling rate, the heat lost by a lava flow, should remain relatively constant for the range of eruption conditions on the NEPR. Gentle, effusive underwater eruptions may lose a lot of heat initially, but quickly form a thick insulating crust that reduces the cooling rate [*Gregg et al.*, 1996]. Breaking this insulating crust changes the cooling rate and might play some role in distance lava flows can travel, but our study is concerned with lava morphology in the direct vicinity of the eruptive vent. It is difficult to envision how the lava cooling rate might change significantly along the 20 km long third-order segments. Thus the lava cooling rate cannot explain the along-strike differences in lava morphology on the EPR.

[51] Seafloor slope also probably plays very little role in the segment-scale distribution patterns we observe. The crest of the EPR has a remarkably low change in slope along strike throughout our study area; slope gradients of $<1°$ are typical (Figure 6). Slope variations may be the main factor controlling the lava morphology where the slope regionally changes by several degrees, such as on the Puna Ridge or at axial volcanic ridges in the Mid Atlantic Ridge rift valley [e.g., *Smith and Cann*, 1999]. However, no systematic or extensive slope changes occur in our study area that can explain the observed distribution of lava morphology.

[52] Higher viscosity lava is more likely to form pillows while lower viscosity lava is more like to form sheet flows [*Bonatti and Harrison*, 1988]. Either lower temperatures or higher crystal content will increase viscosity. Two independent pieces of evidence suggest that lava viscosity may be higher near volcanic segment ends. First, the lowest Mg

rock samples within a volcanic segment are found near the segment ends (Figure 10). This indicates that lower temperature, higher viscosity eruptions occur at segment ends. Second, the seismic data suggests that the AMC is often disrupted at volcanic segment ends (Table 1). This is consistent with lower geothermal gradient at segment ends, which may result in more cooling of magma passing through this area, and thus higher viscosity lava. *Gregg et al.* [1996] estimated a lava viscosity of ~100 Pa s for the small sheet and lobate eruption at 9°52′N, while *Head et al.* [1996] use a viscosity of ~300 Pa s to model the dominantly pillow constructions on the Mid Atlantic Ridge. Determining the lava viscosity systematically along the NEPR crest over the length of an entire volcanic segment is beyond the scope of this study, but we suggest that variations in range of 100–300 Pa s may contribute to the variation in lava morphology along volcanic segments.

[53] Lava effusion rate, the amount of lava that flows from the eruptive vent per unit time, depends on magma pressure, conduit (dike) width, and magma viscosity. If all other factors are held constant, lower lava effusion rates allow pillow lava to form, while higher effusion rates result in sheet flows [*Griffiths and Fink*, 1992; *Gregg and Fink*, 1995]. The lava effusion rate from a long fissure per unit length of the fissure, Q, is related to dike width, W, by

$$Q = W^3 \Delta P / 12v \quad (1)$$

where ΔP is magma pressure and v is lava viscosity [*Head et al.*, 1996]. Magmatic overpressure in the AMC is likely to be the main factor controlling effusion rate because it contributes both to the effusion rate directly, and to the width that the dike walls are forced apart [e.g., *Rubin*, 1995; *Head et al.*, 1996]. However, changes in magmatic overpressure on the EPR have never been measured directly. This underscores the need for detailed geodetic measurements that could detect changes in the state of the AMC over time. The magma pressure, ΔP, driving an eruption on the EPR fed from the AMC may be simplified to an analytic equation:

$$\Delta P = \rho_c g Z + \Delta P_m - \rho_m g Z - \gamma Z, \quad (2)$$

where ρ_c is the bulk density of the overlying crust, ρ_m is the density of the magma, g is the gravitational acceleration, Z is the depth to the AMC, ΔP_m is the overpressure in the magma chamber, and γ is the dynamic pressure required to drive magma up the dike [*Buck et al.*, 1997; *Jaupart*, 2000]. *Buck et al.* [1997] found that the extrusive:intrusive thickness ratio above the AMC was self-regulating to keep the bulk density of overlying crust close to the magma density, effectively canceling the first and third terms of equation 2. The pressure required to push magma up a dike against viscous resistance to flow is probably ~1 MPa for an AMC at ~1.5 km below seafloor, but it is also inversely related to dike width cubed for a Bingham magma rheology [*Hardee*, 1987; *Buck et al.*, 1997; *Jaupart*, 2000]. A variation in the depth of the AMC below the seafloor by ~100 m could change the magma pressure by ~0.1 MPa in a 1 m wide dike. The structure of the AMC correlates with volcanic segmentation, but depth changes are probably relatively small (~100 m or less). We speculate that disruptions in the AMC may reduce ΔP by increasing AMC depth or decreasing dike width. This would lead to reduced volcanic effusion rates and a tendency to form pillow lavas at volcanic segment ends.

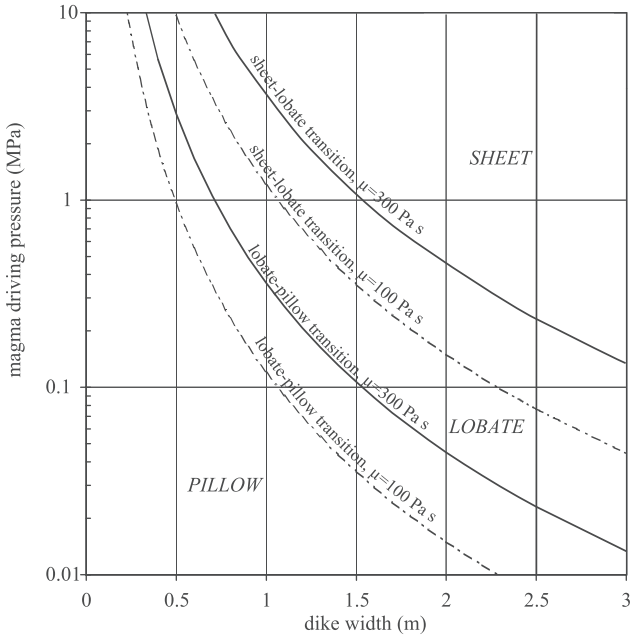

Figure 11. Driving pressure at the volcanic vent needed to erupt a lava morphology for a geologically reasonable range of feeder dike widths. Divisions between pillow, lobate, and sheet flows are calculated for the effusion rate of the transitions between lava morphologies during a fissure eruption for both 100 Pa s (dashed line) and 300 Pa s (solid line) viscosity basalt from *Gregg and Fink* [1995]. The prevalence of lobate lava in the study area is reasonable for dike widths of 1–2 m and driving pressures of ~1 MPa. Morphology from pillow to sheet lava flows can be produced by small variations in driving pressure and lava viscosity within estimated range of variation (discussed in the text).

[54] How much does lava viscosity or effusion rate have to vary to account for the range of lava morphology? We need to relate effusion rate to viscosity, and then relate both to lava morphology in order to address this question. *Gregg and Fink* [1995] found a linear relationship between viscosity and effusion rate that would reasonably model the transition between different lava morphology types found on mid-ocean ridges. Assuming a basaltic viscosity between 100 Pa s [*Gregg et al.*, 1996] and 300 Pa s [*Head et al.*, 1996], we determine the approximate effusion rate for the pillow-lobate and lobate-sheet transitions from *Gregg and Fink* [1995] as $\sim 10^1$ m^3/s and $\sim 10^3$ m^3/s respectively. We then apply equation 1 to calculate the relationship between dike width and magma pressure at our two assumed viscosities (Figure 11). Although we have limited constraints, ΔP is likely to be within an order of magnitude of 1 MPa based on our earlier estimates. Dike widths from 0.5 to 2 m are most commonly seen in analogue crustal sections [*Karson*, 1998; *Karson et al.*, 1992, 1999]. Morphology from pillow to sheet lava flows can be produced by variations of the parameters in equation (1) within geologically reasonable ranges (Figure 11). This supports our

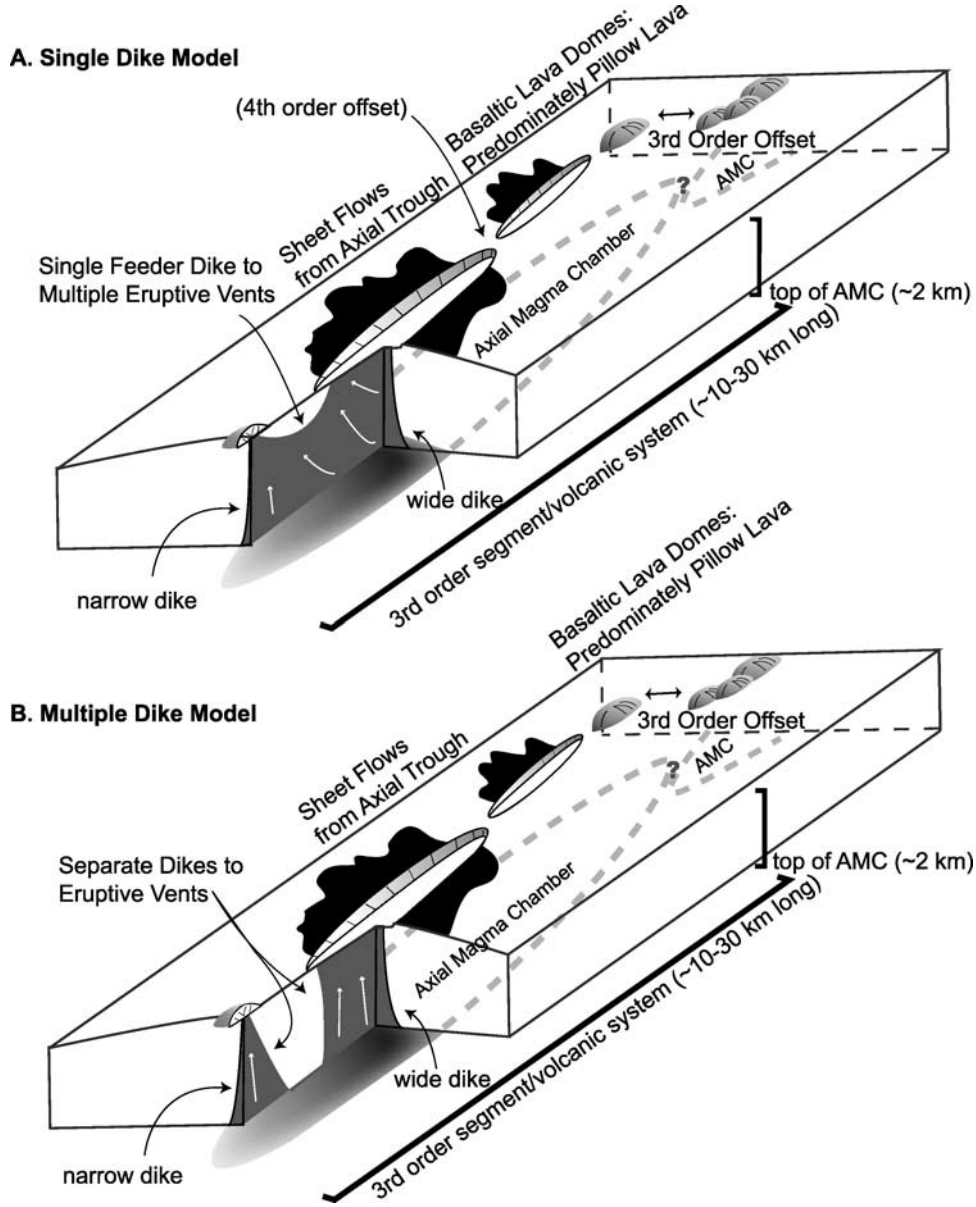

Figure 12. Conceptual block diagrams of the trends observed in volcanic morphology along the ridge crest and underlying volcanic plumbing systems. The important difference between these two models is dike propagation. White arrows show hypothesized magma flow paths within the dikes. (a) Model showing a single, long dike propagates from near mid-segment erupting contemporaneously near segment center and end. (b) Model depicting separate short dikes, which do not propagate far along-axis, feeding separate eruptions along the third-order segment. In both cases dikes may be narrower and tap into a smaller, colder axial magma chamber (AMC) near third-order segment ends, thus creating the tendency for relatively lower effusion rate/higher viscosity eruptions near the ends compared to the centers of third-order segments. The AMC is illustrated dashed lines where it lies underneath the block model and shading. Seismic data indicate a discontinuity at the level of the AMC coincides with third-order segment ends (marked with a question mark) (Table 1). Most fourth-order discontinuities, such as the gap between axial troughs, are not associated with changes in volcanic morphology or discontinuities in the AMC. These two models represent end-members of the style of eruptive dikes feeding eruptions on the EPR that need not be mutually exclusive.

view that lava viscosity and effusion rate are the two main factors controlling the distribution of lava morphology along volcanic segments.

[55] Near volcanic segment centers, especially within the ASCT, eruptions produce few to no pillow lava flows. Perhaps the reason is that eruptions catastrophically and suddenly cease when the threshold for viscous transport in the magma column is reached while magma driving pressure is still too high to produce pillow flows. This may occur near segment centers due to some combination of

wider dikes and lower lava viscosity. For example, the driving pressure must fall well below 0.1 MPa for >1 m wide dike erupting 100 Pa s viscosity lava to form pillow flows (Figure 11). Such a low driving pressure may be below the minimum needed to sustain the eruption.

[56] The nearly constant average thickness of the volcanic layer (measured by the thickness of seismic layer 2A [*Harding et al.*, 1993]) over the length of volcanic segments implies that eruptions must deposit nearly equal thickness of lava at volcanic segment ends and segment centers. If effusion rate controls lava morphology, either eruptions must be longer-lived and more frequent at volcanic segment ends than at segment centers, or more lava is erupted near segment centers than at segment ends but not deposited on-axis there. Lava may tend to flow farther off-axis near segment centers than at segment ends. The volume of excess lava that needs to be transported off axis at segment centers to maintain a constant volcanic layer thickness depends on the differences in the frequency of eruptions as well as the integrated effusion rates at segment end and center. An alternative explanation for constant volcanic layer thickness is that lava viscosity plays the main role in controlling lava morphology and effusion rate remains relatively constant.

[57] In summary, lava viscosity and lava effusion rate are the factors probably controlling the variation of lava morphology within volcanic segments on the EPR. Neither cooling rate nor seafloor slope can plausibly account for along-strike variations in lava morphology of the EPR that correlates with volcanic segmentation. Factors controlling lava morphology (pressure and viscosity of magma within the eruption conduit) are ultimately controlled by the magma source and the path of the dike from source to seafloor surface. The seismic (Table 1) and geochemical (Figure 10) evidence are consistent with a smaller volume, lower temperature, poorly interconnected magma plumbing system near third-order segment boundaries at the level of the AMC. We envision two scenarios for the volcanic plumbing system between the AMC and seafloor: segment-length dikes and short dikes (Figure 12). In one scenario (Figure 12a), long dikes propagate along-axis and upward from volcanic segment centers, so that eruptions near the volcanic segment ends tend to come from the vicinity of the propagating tip. Thus, near the segment end, the dike is narrowest, the magma farthest-traveled, and low effusion rate eruptions are common. A propagating dike, similar to what we envision for the NEPR, was suggested to account for the high levels of hydrothermal activity near the center and the formation of pillow lava mounds at the end of the northern Cleft segment of the Juan de Fuca ridge [*Embley and Chadwick*, 1994]. In the other scenario (Figure 12b), dikes are much shorter and do not propagate along axis. Shorter along axis dike lengths, narrower dike widths, lower magma driving pressures, and higher magma viscosities are also consistent with eruption from smaller, cooler magma sources expected near volcanic segment ends.

7. Conclusions

[58] Several new conclusions about the nature of volcanic systems at fast spreading ridges result from this study of the distribution of volcanic structures and lava flow morphology on the EPR.

1. The third-order ridge discontinuities in the ridge crest bathymetry correspond to areas along the ridge crest where volcanic structures (axial lava domes and breaks in the ASCT) and lava flow morphology (increased abundance of pillow lava flows) indicate reduced eruption effusion rates and/or higher lava viscosities. We infer that disruptions in the volcanic plumbing system delivering lava to eruptive vents cause these changes.

2. Lobate lava flows are the most common lava morphology within the study areas on both the northern and southern EPR, but regional variations in the abundance of sheet flows and pillow flows are important indicators of the variation in eruptive style.

3. Pillow lava flows are nearly twice as abundant on the EPR at 9°–10°N and at 17°–18°S [*White et al.*, 2000] as previously thought for fast spreading ridges [*Bonatti and Harrison*, 1988], but their distribution is strongly concentrated toward ridge discontinuities.

4. Axial pillow lava domes at 9°–10°N are rare in comparison to the southern EPR [*White et al.*, 2000]. However, the few lava domes that exist at 9°–10°N are closely associated with third-order segment ends.

5. Volcanic segmentation corresponds to third-order ridge segmentation on both the northern and southern EPR. The distribution of volcanic structures and lava flow morphology observed on both the northern and southern EPR implies that decreased eruption effusion rates or increased lava viscosity near third-order segment ends is characteristic of fast spreading ridges.

6. No volcanic segment boundaries exist where the ASCT is a continuous structure. However, two gaps in the ASCT (the fissured relay zone at 9°43.5′–45′N and the overlapping troughs around 9°37′N) correspond to volcanic segment boundaries.

7. Consistent patterns in lava dome and lava morphology distribution in the axial zone that emerge when multiple third-order segments are stacked to average their random variations in space and time suggest that volcanic segmentation persists over several individual eruptive episodes.

8. Discontinuities in the AMC and along axis geochemical variations correlate with volcanic segmentation. From this we infer that the volcanic segmentation is influenced directly by segmentation of magma supply at 1–2 km below seafloor.

9. Volcanic systems segmented by third-order discontinuities are estimated to last 10^4–10^5 years, 1–3 orders of magnitude longer than hydrothermal systems segmented by fourth-order discontinuities *Haymon* [1996] that last 10^2–10^3 years.

[59] **Acknowledgments.** Data for this study were collected on Venture III on the R/V *Washington* in 1989 and Nemo 2 on R/V *Melville* in 2000. We thank the captains, crews, and scientists for their outstanding work during those legs. We thank the WHOI Deep Submergence Operations Group, especially S. Gegg, B. Elder, P. Bernard, T. Crook, C. Elder, and J. Keeler, for the operation of the DSL-120 vehicle and sonar system. The swift post-processing of the DSL-120 sonar data while at sea by S. Gegg, P. Johnson, G. Kurras, and J. Getsiv contributed greatly to the completion of this study. Special thanks to Brooke Stembridge for entering all the 1989 *Argo I* lava morphology data into our GIS database. We thank S. Carbotte, J. Engles, G. Kurras, M. Smith, K. Sims, M. Tolstoy, D. Wilson, and D. Wright for

constructive discussions and assistance with this study. We thank M. Tivey, D. Smith, and T. Gregg for constructive and careful reviews. This study was funded by grants OCE88-17587 (R.M.H.), OCE94-16996 (R.M.H.), OCE94-02360 (M.R.P.), OCE94-03773 (M.R.P.), OCE98-16021 (K.C.M.), N00014-93-1-0108 (K.C.M.), N00014-94-10678 (K.C.M.).

References

Auzende, J. M., V. Ballu, R. Batiza, D. Bideau, J. L. Charlou, M.-H. Cormier, Y. Fouquet, P. Geistdoerfor, Y. Lagabrielle, J. Sinton, and P. Spadea, Recent tectonic, magmatic and hydrothermal activity on the East Pacific Rise between 17° and 19°S: Submersible observations, *J. Geophys. Res.*, *101*(B8), 17,995–18,010, 1996.

Batiza, R., and Y. Niu, Petrology and magma chamber processes at the East Pacific Rise ~9°30′N, *J. Geophys. Res.*, *97*(B5), 6779–6797, 1992.

Bonatti, E., and C. G. A. Harrison, Eruption style of basalt in oceanic spreading ridges and seamounts: Effect of magma temperature and viscosity, *J. Geophys. Res.*, *93*(B4), 2967–2980, 1988.

Buck, W. R., S. M. Carbotte, and C. Mutter, Controls on extrusion at mid-ocean ridges, *Geology*, *25*(10), 935–938, 1997.

Carbotte, S. M., and K. C. Macdonald, East Pacific Rise 8°–10°30′N: Evolution of ridge segments and discontinuities from SeaMARC II and three-dimensional magnetic studies, *J. Geophys. Res.*, *97*(B5), 6959–6982, 1992.

Carbotte, S. M., and K. C. Macdonald, The axial topographic high at intermediate and fast spreading ridges, *Earth Planet. Sci. Lett.*, *128*, 85–97, 1994.

Carbotte, S. M., A. Solomon, and G. Ponce-Correa, Evaluation of morphological indicators of magma supply and segmentation from a seismic reflection study of the East Pacific Rise, 15 30′–17 N, *J. Geophys. Res.*, *105*(B2), 2737–2760, 2000.

Cochran, J. R., D. J. Fornari, B. J. Coakley, R. Herr, and M. A. Tivey, Continuous near-bottom gravity measurements made with a BGM-3 gravimeter in DSV *Alvin* on the East Pacific Rise near 9 degree 31′N and 9 degrees 50′N, *J. Geophys. Res.*, *104*(B5), 10,841–10,861, 1999.

Cormier, M.-H., D. S. Scheirer, and K. C. Macdonald, Evolution of the East Pacific Rise at 16°–19°S since 5 Ma: Bisection of OSC's by new rapidly propagating ridge segments, *Mar. Geophys. Res.*, *18*(1), 52–84, 1996.

Detrick, R. S., P. Buhl, E. Vera, J. Mutter, J. Orcutt, J. Madsen, and T. Brocher, Multi-channel seismic imaging of a crustal magma chamber along the East Pacific Rise, *Nature*, *326*, 35–41, 1987.

Dunn, R. A., D. R. Toomey, and S. C. Solomon, Three-dimensional seismic structure and physical properties of the crust and shallow mantle beneath the East Pacific Rise at 9 30′N, *J. Geophys. Res.*, *105*, 23,537–23,556, 2000.

Eberle, M. A., and D. W. Forsyth, An alternative dynamic model of the axial topographic high at fast spreading ridges, *J. Geophys. Res.*, *103*(B6), 12,309–12,320, 1998.

Embley, R. W., and W. W. Chadwick, Volcanic and hydrothermal processes associated with a recent phase of seafloor spreading at the northern Cleft segment: Juan de Fuca Ridge, *J. Geophys. Res.*, *99*(B3), 4741–4760, 1994.

Embley, R. W., W. W. Chadwick, M. R. Perfit, M. C. Smith, and J. R. Delaney, Recent eruptions on the CoAxial segment of the Juan de Fuca ridge: Implications for mid-ocean ridge accretion processes, *J. Geophys. Res.*, *105*(B7), 16,501–16,526, 2000.

Fornari, D. J., R. M. Haymon, M. R. Perfit, T. K. P. Gregg, and M. H. Edwards, Axial summit trough of the East Pacific Rise 9°N to 10°N: Geological characteristics and evolution of the axial zone on fast-spreading mid-ocean ridges, *J. Geophys. Res.*, *103*(B5), 9827–9855, 1998.

Gente, P., J. M. Auzende, V. Renare, Y. Fouquet, and D. Bideau, Detailed geological mapping by submersible of the East Pacific Rise axial graben near 13°N, *Earth. Planet. Sci. Lett.*, *78*, 224–236, 1986.

Gregg, T., and W. Chadwick, Submarine lava-flow inflation; a model for the formation of lava pillars, *Geology*, *24*, 981–984, 1996.

Gregg, T. K. P., and J. H. Fink, Quantification of submarine lava-flow morphology through analog experiments, *Geology*, *23*, 73–76, 1995.

Gregg, T. K. P., D. J. Fornari, M. R. Perfit, R. M. Haymon, and J. H. Fink, Rapid emplacement of a mid-ocean ridge lava flow on the East Pacific Rise at 9°46′–51′N, *Earth Planet. Sci. Lett.*, *144*, E1–E7, 1996.

Griffiths, R. W., and J. A. Fink, Solidification and morphology of submarine lavas; a dependence on extrusion rate, *J. Geophys. Res.*, *97*(B13), 19,729–19,737, 1992.

Gudmundsson, A., Infrastructure and mechanics of volcanic systems in Iceland, *J. Volcanol. Geotherm. Res.*, *64*, 1–22, 1995.

Hardee, H. C., Heat and mass transport in the east-rift-zone magma conduit of Kilauea Volcano, in *Volcanism in Hawaii,* edited by R. W. Decker, T. L. Wright, and P. H. Stauffer, *U.S. Geol. Surv. Prof. Pap., 1350*, 1471–1486, 1987.

Harding, A. J., G. M. Kent, and J. A. Orcutt, A multichannel seismic investigation of upper crustal structure at 9°N on the East Pacific Rise: Implications for crustal accretion, *J. Geophys. Res.*, *98*(B8), 13,925–13,944, 1993.

Haymon, R., The response of ridge-crest hydrothermal systems to segmented, episodic magma supply, in *Tectonic, Magmatic, Hydrothermal and Biological Segmentation of Mid-Ocean Ridges*, edited by C. J. MacLeod, P. A. Tyler, and C. L. Walker, *Geol. Soc. Spec. Publ., 118*, 157–168, 1996.

Haymon, R. M., D. J. Fornari, M. H. Edwards, S. Carbotte, D. Wright, and K. C. Macdonald, Hydrothermal vent distribution along the East Pacific Rise Crest (9°09′–54′N) and its relationship to magmatic and tectonic processes on fast-spreading mid-ocean ridges, *Earth Planet. Sci. Lett.*, *104*, 513–534, 1991.

Haymon, R. M., et al., Volcanic eruption of the mid-ocean ridge along the East Pacific Rise crest at 9°45′–52′N: Direct submersible observations of seafloor phenomena associated with an eruption event in April, 1991, *Earth Planet. Sci. Lett.*, *119*, 85–101, 1993.

Head, J. W., L. Wilson, and D. K. Smith, Mid-ocean ridge eruptive vent morphology and substructure: Evidence for dike widths, eruption rates, and the evolution of eruptions and axial volcanic ridges, *J. Geophys. Res.*, *101*(B12), 28,265–28,280, 1996.

Jaupart, C., Magma ascent at shallow levels, in *Encyclopedia of Volcanoes*, edited by H. Sigurdsson, pp. 237–245, Academic, San Diego, Calif., 2000.

Karson, J. A., Internal structure of oceanic lithosphere: A perspective from tectonic windows, in *Faulting and Magmatism at Mid-ocean Ridges*, *Geophys. Monogr. Ser.*, vol. 106, edited by W. R. Buck et al., pp. 177–218, AGU, Washington, D. C., 1998.

Karson, J. A., S. D. Hurst, and P. Lonsdale, Tectonic rotations of dikes in fast-spread oceanic crust exposed near Hess Deep, *Geology*, *20*, 685–692, 1992.

Karson, J. A., E. M. Klein, S. D. Hurst, and H.D.S.P., Internal structure of uppermost fast-spread oceanic crust of the East Pacific Rise exposed at the Hess Deep rift: Results from *Alvin*, *Argo II*, and DSL-120 investigations, *Eos Trans. AGU*, *80*(46), Fall Meet. Suppl., F983, 1999.

Kastens, K. A., W. B. F. Ryan, and P. J. Fox, Structural and volcanic expression of a fast slipping ridge-transform-ridge-plate boundary: Sea MARC I and photographic surveys of the Clipperton Transform Fault, *J. Geophys. Res.*, *91*, 3469–3488, 1986.

Kent, G., A. J. Harding, and J. A. Orcutt, Distribution of magma beneath the East Pacific Rise between the Clipperton Transform and the 9°17′N deval from forward modeling of common depth point data, *J. Geophys. Res.*, *98*(B8), 13,945–13,969, 1993a.

Kent, G., A. J. Harding, and J. A. Orcutt, Distribution of magma beneath the East Pacific Rise near the 9°03′N overlapping spreading center from forward modeling of common depth point data, *J. Geophys. Res.*, *98*(B8), 13,971–13,995, 1993b.

Kurras, G. J., D. F. Fornari, M. F. Edwards, M. R. Perfit, and M. C. Smith, Volcanic morphology of the East Pacific Rise crest 9°49′–52′N: Implications for volcanic emplacement processes at fast-spreading mid-ocean ridges, *Mar. Geophys. Res.*, *21*, 23–41, 2000.

Langmuir, C. H., J. F. Bender, and R. Batiza, Petrological and tectonic segmentation of the East Pacific Rise, 5°30′N–14°30′N, *Nature*, *322*, 422–429, 1986.

Lee, S.-M., S. C. Solomon, and M. A. Tivey, Fine-scale crustal magnetization anomalies and segmentation of the East Pacific rise, 9°10′–9°50′N, *J. Geophys. Res.*, *101*(B10), 22,033–22,050, 1996.

Macdonald, K. C., and P. J. Fox, The axial summit graben and cross-sectional shape of the East Pacific Rise as indicators of axial magma chambers and recent volcanic eruptions, *Earth Planet. Sci. Lett.*, *88*, 119–131, 1988.

Macdonald, K. C., J.-C. Sempere, and P. J. Fox, East Pacific Rise from Siqueiros to Orozco Fracture Zones: Along-strike continuity of axial neovolcanic zone and structure and evolution of overlapping spreading centers, *J. Geophys. Res.*, *89*(B7), 6049–6069, 1984.

Macdonald, K. C., P. J. Fox, L. J. Perram, M. F. Eisen, R. M. Haymon, S. P. Miller, S. M. Carbotte, M.-H. Cormier, and A. N. Shor, A new view of the mid-ocean ridge from the behaviour of ridge-axis discontinuities, *Nature*, *335*, 217–225, 1988.

Macdonald, K. C., P. J. Fox, S. Carbotte, M. Eisen, S. Miller, L. Perram, D. Scheirer, S. Tighe, and C. Weiland, The East Pacific Rise and its flanks, 8°–18°N: History of segmentation, propagation and spreading direction based on SeaMARC II and Sea Beam studies, *Mar. Geophys. Res.*, *14*, 299–344, 1992.

Madsen, J. A., R. Detrick, T. Brocker, P. Buhl, J. Mutter, and J. Orcutt, Variations in the morphology and isostasy of the East Pacific Rise between 9° and 14°N, *Eos Trans. AGU*, *67*, 360, 1986.

McConachy, T. F., R. D. Ballard, M. J. Mottl, and R. P. Von Herzen, Geologic form and setting of a hydrothermal vent field at 10°56′N, East

Pacific Rise: A detailed study using ANGUS and ALVIN, *Geology*, *14*, 295–298, 1986.

Miller, T. P., R. G. McGimsey, D. H. Richter, J. R. Riehle, C. J. Nye, M. E. Yount, and J. A. Dumoulin, Catalog of historically active volcanoes of Alaska, *U.S. Geol. Surv. Open File Rep., 98-582*, 104 pp., 1998.

Perfit, M. R., and W. W. Chadwick, Magmatism at mid-ocean ridges: constraints from volcanological and geochemical investigations, in *Faulting and Magmatism at Mid-ocean Ridges*, *Geophys. Monogr. Ser.*, vol. 106, edited by W. R. Buck et al., pp. 59–116, AGU, Washington, D. C., 1998.

Perfit, M. R., D. J. Fornari, M. C. Smith, J. F. Bender, C. H. Langmuir, and R. M. Haymon, Small-scale spatial and temporal variations in mid-ocean ridge crest magmatic processes, *Geology*, *22*, 375–379, 1994.

Renard, V., R. Hekinian, J. Francheteau, R. D. Ballard, and H. Backer, Submersible observations at the axis of the ultra fast spreading East Pacific Rise (17°30′ to 21°30′S), *Earth Planet. Sci. Lett.*, *88*, 339–353, 1985.

Rossi, M. J., Morphology and mechanism of eruption of postglacial shield volcanoes in Iceland, *Bull. Volcanol.*, *57*(7), 530–540, 1996.

Rubin, A. M., Propagation of magma-filled cracks, *Annu. Rev. Earth Planet. Sci.*, *23*, 287–336, 1995.

Scheirer, D. S., and K. C. Macdonald, Variation in cross-sectional area of the axial ridge along the East Pacific Rise: Evidence for the magmatic budget of a fast-spreading center, *J. Geophys. Res.*, *98*(B5), 7871–7885, 1993.

Scheirer, D. S., D. J. Fornari, S. E. Humphris, and S. Lerner, High-resolution seafloor mapping using the DSL-120 sonar system: Quantitative assessment of sidescan and phase-bathymetry data from the Lucky Strike segment of the Mid-Atlantic Ridge, *Mar. Geophys. Res.*, *21*, 121–142, 2000.

Simkin, T., and L. Siebert, Earth's volcanoes and eruptions: An overview, in *Encyclopedia of Volcanoes*, edited by H. Sigmundsson, pp. 249–262, Academic, San Diego, Calif., 2000.

Sims, K. W., et al., Chemical and isotopic constraints on the generation and transport of magma beneath the East Pacific Rise, *Geochim. Cosmochim. Acta*, in press, 2002.

Singh, S. C., G. M. Kent, J. S. Collier, A. J. Harding, and J. A. Orcutt, Melt to mush variations in crustal magma properties along the ridge crest at the southern East Pacific Rise, *Nature*, *394*, 874–878, 1998.

Sinton, J. M., and R. S. Detrick, Mid-ocean ridge magma chambers, *J. Geophys. Res.*, *97*(B1), 197–216, 1992.

Smith, D. K., and J. R. Cann, Constructing the upper crust of the Mid-Atlantic Ridge: A reinterpretation based on the Puna Ridge, Kilauea Volcano, *J. Geophys. Res.*, *104*(B11), 25,379–25,400, 1999.

Smith, D. K., J. R. Cann, M. E. Dougherty, J. Lin, S. Spencer, C. MacLeod, J. Keeton, E. McAllister, B. Brooks, R. Pascoe, and W. Robertson, Mid-Atlantic Ridge volcanism from deep-towed side-scan sonar images, 25–29N, *J. Volcanol. Geotherm. Res.*, *67*, 233–262, 1995.

Smith, M. C., M. R. Perfit, D. J. Fornari, W. I. Ridley, M. H. Edwards, G. Kurras, and K. L. Von Damm, Magmatic processes and segmentation at a fast spreading mid-ocean ridge: Detailed investigation of an axial discontinuity on the East Pacific Rise crest at 9°37′N, *Geochem. Geophys. Geosyst.*, *2*(Article), 2000GC000134[15,977 words], 2001.

Smellie, J. R., I. L. Millar, D. C. Rex, and P. J. Butterworth, Subaqueous, basaltic lava dome and carapace breccia on King George Island, South Shetland Islands, Antarctica, *Bull. Volcanol.*, *59*, 245–261, 1998.

Stewart, K. W., D. Chu, S. Malik, S. Lerner, and H. Singh, Quantitative seafloor characterization using a bathymetric sidescan sonar, *IEEE J. Oceanic Eng.*, *19*, 599–610, 1994.

Toomey, D. R., G. M. Purdy, S. C. Solomon, and W. S. Wilcock, The three-dimensional seismic velocity structure of the East Pacific Rise near latitude 9°30′N, *Nature*, *347*, 639–645, 1990.

Toomey, D. R., S. C. Solomon, and G. M. Purdy, Tomographic imaging of the shallow crustal structure of the East Pacific Rise at 9°30′N, *J. Geophys. Res.*, *99*(B12), 24,135–24,157, 1994.

Vera, E. E., and J. B. Diebold, Seismic imaging of oceanic layer 2A between 9°30′N and 10°N on the East Pacific Rise from two-ship wide-aperture profiles, *J. Geophys. Res.*, *99*(B2), 3031–3041, 1994.

Von Damm, K. L., Chemistry of hydrothermal vent fluids from 9°–10°N, East Pacific Rise: ''Time zero,'' the immediate posteruptive period, *J. Geophys. Res.*, *105*(B5), 11,203–11,222, 2000.

Von Damm, K. L., S. E. Oosting, R. Kozlowski, L. G. Buttermore, M. D. Lilley, E. J. Olson, and E. McLaughlin, Evolution of East Pacific Rise hydrothermal vent fluids following a volcanic eruption, *Nature*, *375*, 47–50, 1995.

White, S. M., K. C. Macdonald, and R. M. Haymon, Basaltic lava domes, lava lakes, and volcanic segmentation of the southern East Pacific Rise, *J. Geophys. Res.*, *105*(B10), 23,519–23,536, 2000.

Wilcock, W. S. D., D. R. Toomey, G. M. Purdy, and S. C. Solomon, The renavigation of Sea Beam bathymetric data between 9°N and 10°N on the East Pacific Rise, *Mar. Geophys. Res.*, *15*, 1–12, 1993.

Williams, H., The history and character of volcanic domes, *Bull. Dep. Geol. Sci. Univ. Calif. Publ.*, *21*, 51–146, 1932.

Wright, D. J., R. M. Haymon, and D. J. Fornari, Crustal fissuring and its relationship to magmatic and hydrothermal processes on the East Pacific Rise crest (9°12′ to 54′N), *J. Geophys. Res.*, *100*(B4), 6097–6120, 1995.

D. J. Fornari, Department of Geology and Geophysics, Woods Hole Oceanographic Institution, Clark S 172, MS 22, Woods Hole, MA 02543-1052, USA. (dfornari@whoi.edu)

R. M. Haymon and K. C. Macdonald, Department of Geological Sciences and Marine Science Institute, University of California, Santa Barbara, CA 93106, USA. (haymon@geol.ucsb.edu; macdonald@geol.ucsb.edu)

M. R. Perfit, Department of Geological Sciences, University of Florida, 241 Williamson Hall, P.O. Box 112120, Gainesville, FL 32611-2120, USA. (perfit@geology.ufl.edu)

S. M. White, Department of Geological Sciences, University of South Carolina, 701 Sumter Street, Columbia, SC 29208, USA. (swhite@geol.sc.edu)